minerals

MDPI

Article

Dating Metasomatism: Monazite and Zircon Growth during Amphibolite Facies Albitization

Cailey B. Condit [1,*], Kevin H. Mahan [2], Kelly C. Curtis [2] and Andreas Möller [3]

1 Department of Earth, Environmental and Planetary Sciences, Rice University, Houston 77005, TX, USA
2 Department of Geological Sciences, University of Colorado, Boulder 80309, CO, USA; kevin.mahan@colorado.edu (K.H.M.); Kelly.Curtis@colorado.edu (K.C.C.)
3 Department of Geology, The University of Kansas, Lawrence 66045, KS, USA; amoller@ku.edu
* Correspondence: cailey.condit@rice.edu

Received: 24 March 2018; Accepted: 24 April 2018; Published: 29 April 2018

Abstract: We present coupled textural observations and trace element and geochronological data from metasomatic monazite and zircon, to constrain the timing of high-grade Na-metasomatism (albitization) of an Archean orthogneiss in southwest Montana, USA. Field, mineral textures, and geochemical evidence indicate albitization occurred as a rind along the margin of a ~3.2 Ga granodioritic orthogneiss (Pl + Hbl + Kfs + Qz + Bt + Zrn) exposed in the Northern Madison range. The metasomatic product is a weakly deformed albitite (Ab + Bt + OAm + Zrn + Mnz + Ap + Rt). Orthoamphibole and biotite grew synkinematically with the regional foliation fabric, which developed during metamorphism that locally peaked at upper amphibolite-facies during the 1800–1710 Ma Big Sky orogeny. Metasomatism resulted in an increase in Na, a decrease in Ca, K, Ba, Fe, and Sr, a complete transformation of plagioclase and K-feldspar into albite, and loss of quartz. In situ geochronology on zoned monazite and zircon indicate growth by dissolution–precipitation in both phases at ~1750–1735 Ma. Trace element geochemistry of rim domains in these phases are best explained by dissolution–reprecipitation in equilibrium with Na-rich fluid. Together, these data temporally and mechanistically link metasomatism with high-grade tectonism and prograde metamorphism during the Big Sky orogeny.

Keywords: metasomatism; albitization; geochronology; trace element geochemistry; monazite; zircon; SW Montana

1. Introduction

Fluids can significantly influence the chemical characteristics and rheological behavior of the deep crust and lithosphere. Metasomatic alteration can locally affect processes such as strain concentrations and gradients, due to shifts in rheological properties [1–3], and material transport via vein formation and ore deposition [4]. Regionally high fluid fluxes can catalyze metamorphism [5], and have much larger scale effects, such as transformation of the density structure of the lithosphere [6–8]. Within subduction zone systems, fluids transport large amounts of solute, efficiently silicifying overriding crust (e.g., [9]), a process which can influence mechanical plate behaviors [10].

Establishing the ambient conditions under which alteration occurs, the origin of the fluids, and the timing of metasomatism are all important aspects that facilitate understanding these geologic processes. However, these variables can be difficult to constrain. Obtaining pressure-temperature (P-T) conditions of metasomatism is often a challenge, due to convoluted or unclear overprinting relationships between fluid alteration conditions and prior or subsequent metamorphism, making it problematic to apply traditional thermobarometry to these kinds of rocks [11]. Identifying fluid sources that catalyze these alterations can be difficult, particularly where fluid inclusions of the primary

metasomatic agent are lacking [12]. Pinpointing the exact timing of metasomatism also remains a difficult task, often because of the multidomainal nature of metasomatic phases, phase growth via dissolution–precipitation, and the difficulties inherent in distinguishing datable phase (e.g., zircon, monazite) growth as fluid-related, rather than closed system metamorphism [13]. Constraints on the timing of metasomatism are often best provided by integrating textural, morphological, geochronologic, and geochemical analysis of accessory mineral phases [14–16]. It is this last challenge that we focus on for this contribution: providing robust geochronological constraints on metasomatism and fluid alteration.

Albitization is a common metasomatic process by which Na-rich fluid infiltration leads to the alteration of granitoids and metasedimentary rocks, transforming feldspar of variable compositions into more albitic feldspar [17]. During the transformation of calcic plagioclase into albite, quartz will also be consumed [18], and marked increases in Na and decreases in K, Rb, Ba, and Ca in the bulk rock composition are common. Albitization can occur over a range of crustal conditions, from diagenetic to upper amphibolite and even granulite facies (e.g., [19]).

In this contribution, we evaluate the origin of an albitite that occurs in the Precambrian rocks of the Northern Madison Range in Southwest Montana. We consider both metasomatic and magmatic mechanisms of formation, and present field observations, geochemical data, and monazite and zircon morphology, textures, geochronology, and geochemistry. The results indicate that fluid flow and localized metasomatism of the margin of an Archean granodioritic orthogneiss occurred at 1750–1735 Ma, and establish a temporal link between albitization, metamorphism, and deformation during the Late Paleoproterozoic (~1800–1710 Ma) Big Sky orogeny [20,21]. This implies that local metasomatism and fluid infiltration was active during peak metamorphism and fabric development within this continental collision, rather than magmatic emplacement.

2. Geologic Background

2.1. Regional Geologic Setting

The Precambrian rocks of Southwestern Montana are exposed predominantly in Laramide uplifts and Basin and Range structures (Figure 1A). These consist of Archean to Paleoproterozoic orthogneiss units with several suites of deformed intrusive mafic dikes and interleaved supracrustal metamorphic rocks [21–24]. The majority of these lithologies have Archean protoliths, and along the northwestern margin of the Wyoming province, they contain evidence for at least two high temperature thermotectonic events: the enigmatic 2500–2450 Ma Tobacco Roots–Tendoy orogeny [20,25–27] and the 1800–1710 Ma Big Sky orogeny [20,22], interpreted as the results of the Wyoming province docking with the rest of the Archean core of Laurentia during the amalgamation of supercontinent Nuna [28,29]. To the southeast of the rocks overprinted by Paleoproterozoic thermotectonism, K-Ar and ^{40}Ar-^{39}Ar thermochronology indicates that the Archean rocks have not been thermally overprinted since the Neoarchean (Figure 1A,B; [30–32]).

Rocks in the study area of Bear Basin, located in the Gallatin Peak terrane of the Northern Madison Range (Figure 1B), are composed of quartzofeldspathic orthogneisses, foliated granitoids, amphibolite, quartzite, leucogranite sheet dikes, and intercalated supracrustal schist (Figure 1C; [20,22,33]). Foliated granitoids and orthogneiss units have U-Pb zircon crystallization ages between ~2.8–3.2 Ga [34].

There is evidence of multiple metamorphic events [3], and at least three phases of high-grade deformation in and nearby the northern Gallatin Peak terrane [20,33,35]. The oldest deformation fabrics (D_1) are compositional layered surfaces that are subsequently folded and overprinted by the more pervasive second and third deformational phases. This younger deformation includes regional D_2 and locally occurring D_3 events, both occurring during the late Paleoproterozoic Big Sky orogeny [20]. Major D_2 structures in the region, including map scale folds of earlier D_1 surfaces (Figure 1C), are Northeast–Southwest striking and moderately to steeply southeast dipping foliations, and strong southeast plunging mineral lineations. D_3 structures are limited to local SE-vergent z-folds.

These structures developed between ~1740–1720 Ma at metamorphic conditions of ~0.9 GPa and ~700 °C [20].

The rocks of Bear Basin and the surrounding area preserve field and textural evidence for pervasive fluid flow, including coarse-grained orthoamphibole, garbenschiefer textures within multiple units, and the presence of pervasive hydrous phases. Additional evidence for enhanced flow along some lithologic contacts include metasomatic alteration in the form of garnetiferous regions within typically garnet poor rock types, and the local appearance of kyanite-bearing white colored schists, a rock type that has been interpreted to indicate fluid alteration in other regions [19].

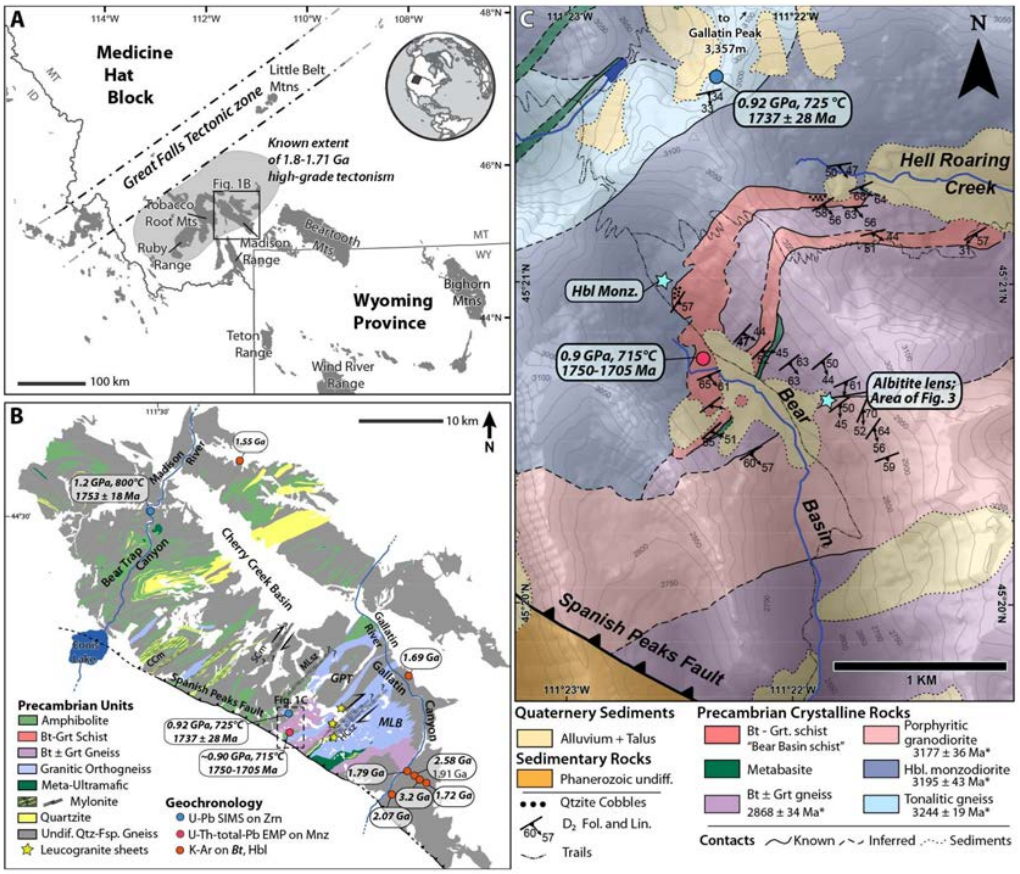

Figure 1. (**A**) Simplified regional geologic map of the northwestern margin of the Wyoming Province, the Great Falls Tectonic zone, and the Medicine Hat Block. Grey shapes are Precambrian-cored basement uplifts; (**B**) Simplified geologic map of the Precambrian-aged rocks in the Northern Madison Range (location inset from (A)). U-Pb geochronologic data from [20] and [36], K-Ar data from [30,31]. CCm—Crooked Creek mylonite, SCm—Spanish Creek mylonite, HCsz—Hellroaring Creek shear zone, MLsz—Mirror Lake shear zone, GPT—Gallatin Peak Terrane, MLB—Moon Lake Block; (**C**) Bedrock geologic map of the Bear Basin region within the Northern Madison Range (location inset from (B)). Red and blue circles show metamorphic pressure–temperature (P-T)-t conditions from [20]. Big Sky-related deformation (D_2 surfaces and lineations) from [20]. Colored stars show locations for samples investigated here, including Hbl monzodiorite and a sequence of samples within and surround the albitite lens spatially detailed further in Figure 3.

2.2. Local Rock Types

Within the Bear Basin region (Figure 1C), the major rock units are dominated by several weakly to moderately foliated Archean orthogneisses. The dates quoted below (at 2σ uncertainty) are from multi-grain zircon U-Pb TIMS analysis by Weyand [34], unless otherwise stated. Along the northern side of the Bear Basin headwall, the oldest unit is a layered tonalitic gneiss with a crystallization age

of 3244 ± 19 Ma. Southeast of the tonalitic gneiss is a weakly foliated Hbl + Pl + Qz +Tnt + Zrn monzodiorite with an age of 3195 ± 43 Ma (abbreviations as defined in [37]). The next youngest unit crops out as a broadly tabular NE-trending body of weakly foliated porphyroclastic granodiorite (Figure 2A,B) in the southern part of the map area in Figure 1C. This unit contains Kfs + Pl + Qz + Hbl + Bt + Zrn, and has a zircon U-Pb crystallization age of 3177 ± 36 Ma. It is generally weakly foliated with a fabric defined by elongate K-feldspar phenocrysts and alignment of amphibole and biotite (Figure 2A,B and Figure 3A). Mogk et al. [38] interpreted these units to represent a ca. 3.2 Ga calc-alkaline continental magmatic arc.

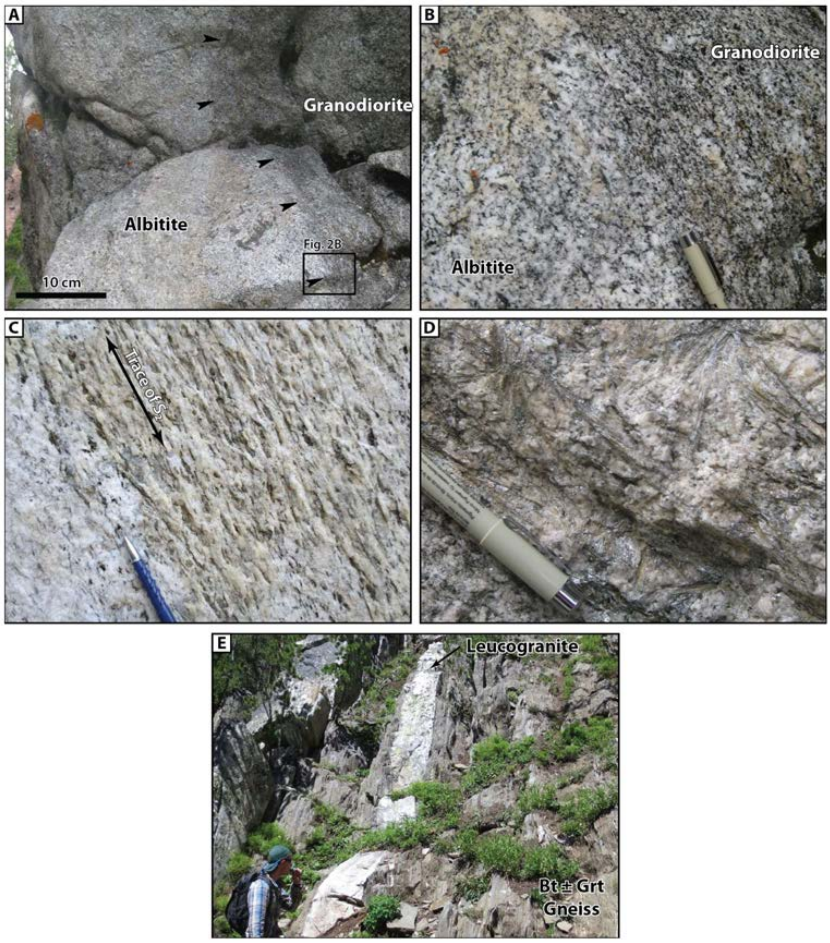

Figure 2. Field photographs of key field relationships and textures: (**A**) Contact between albitite and porphyroclastic granodiorite with black arrows indicating contact location; (**B**) Close up of the contact between the albitite and granodiorite at location indicated in part (A); (**C**) Field photograph of general albitite appearance showing trace of S_2 defined by orthoamphibole and biotite; (**D**) Orthoamphibole garbenschiefer texture within albitite; (**E**) Leucogranite sheets within the Bt ± Grt gneiss. Contacts are concordant with S_2.

The fourth major unit is comprised of intimately mixed and undifferentiated migmatitic biotite schist, granite, and granitic gneiss (Bt ± Grt gneiss in Figure 1C). No structures suggesting a sedimentary origin were recognized within the map area, and no aluminous metamorphic index minerals, other than local garnet, occur. Weyand [34] interprets this unit's protolith as igneous and reports a zircon U-Pb date of 2868 ± 34 Ma. Garnet within this unit is generally small (<500 μm) except along the southeastern contact, where porphyroblasts reach >1.5 cm diameter and occur with garbenschiefer-textured amphibole. In contact with the monzodiorite to the southeast is a Bt + Grt ± Ky ± Sil ± St schist, informally called the Bear Basin schist by Condit et al. [20]. U-Th-total Pb chemical

analysis of monazite yielded dates between ~1750–1705 Ma, interpreted as growth during prograde to peak to retrograde conditions, during D_2 and D_3 fabric development [20]. Condit et al. [20] also dated metamorphic zircon from a nearby deformed mafic dike, which yielded a $^{207}Pb/^{206}Pb$ weighted mean age of 1737 ± 28 Ma.

Minor units that are generally too small to show on the geologic maps include mafic and felsic dikes, as well as the albitite that is the subject of this contribution. This albitite is a lens of white, weakly deformed rock that crops out between the biotite ± garnet gneiss and the porphyroclastic granodiorite (Figures 3 and 4A). Undated leucogranite sheets are 1–5 m wide, generally weakly deformed, and occur locally within the biotite ± garnet gneiss (Figures 1B and 2E). The contacts of these Kfs + Pl + Grt + Bt + Qz + Zrn + Mnz leucogranite sheets are concordant with the regional D_2 foliation surfaces within the gneiss.

3. Albitite

3.1. Field Occurrence

The albitite crops out as a ~10 m wide lens along the northwestern contact of the porphyroclastic granodiorite, locally separating it from the biotite ± garnet gneiss (Figure 1C, Figure 2A,B and Figure 3). Although the contact between the albitite and the gneiss is obscured by a small 2–3 m wide gully, the contact with the granodiorite is well exposed and gradational over several centimeters (Figure 2A,B and Figure 3). Neither unit crosscuts the other, and the contact is approximately parallel to the local orientation of S_2. To the northeast along the strike, the albitite apparently pinches out, while the area below the outcrop is obscured by alluvium. Thus, the albitite is interpreted to have a lenticular 3D shape. The albitite has a weakly developed foliation (parallel to regional S_2) that strikes northeast and dips moderately to the southeast, and contains a mineral lineation defined by orthoamphibole blades and biotite (Figure 2C). Internally, foliation surfaces contain garbenschiefer textures defined by orthoamphibole blades (Figure 2D). Multiple samples were collected in the albitite to evaluate internal variations across the lens, and samples were also collected from both the Bt ± Grt gneiss and the granodiorite, to compare geochemical composition and mineral assemblages. A schematic diagram of the sample positions is shown in Figure 3.

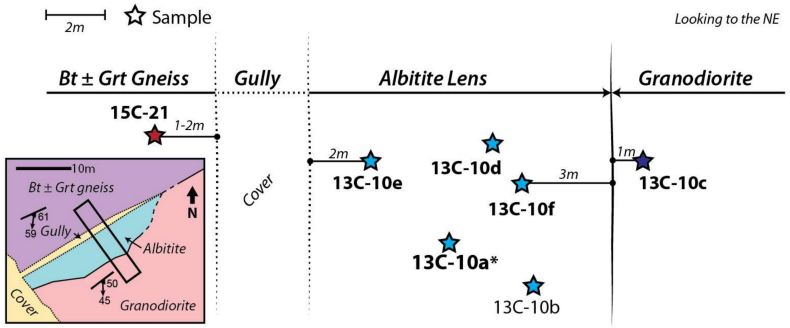

Figure 3. Simplified geologic map and schematic diagram of samples collected across the albitite lens and within the surrounding Bt ± Grt gneiss and porphyroclastic granodiorite. Inset shows geometry of albitite lens, nearby D_2 structural orientations, and location of schematic transect. In the schematic diagram, bold labels indicate samples investigated for accessory mineral (zircon ± monazite) morphology. * indicates sample for which we collected monazite and zircon geochronology and trace element data.

3.2. Mineralogy and Mineral Compositions

Wavelength dispersive spectroscopy (WDS) maps for Ca, Al, Fe and Si, and mineral compositions were collected using the JEOL 8600 Electron Microprobe (EMP) at the University of Colorado Boulder. Beam conditions for X-ray maps were 15 kV voltage, 90 nA current, dwell time of 45 ms/pixel, step size

of 10 µm, and a defocused beam diameter of 10 µm. For quantitative feldspar and orthoamphibole compositions, a 15 kV voltage, 20 nA current, a defocused beam of 5–10 µm, and count times varying from 20–40 s were used. These mineral compositions can be found in Table 1.

The albitite contains Ab + Bt + Oam + Rt + Ap + Mnz + Zrn. Large ~5 mm-scale interlocking plagioclase crystals are interspersed with aligned biotite and elongate orthoamphibole grains approximately 0.5–4 mm long (Figure 4B,C). Albite grain boundaries are often at a high angle to one another (e.g., Figure 4B). Feldspar is almost pure albite (Ab_{94}) (Table 1) and WDS maps show little to no zoning (e.g., Figure 4E). Orthoamphibole is compositionally anthophyllite to Si-rich gedrite (Si = 7.95–6.66 for 24 O, OH, F), (Table 1). Apatite grains are round, up to 400 µm in diameter, and commonly occur adjacent to rutile, monazite, and/or zircon. The albitite is rich in accessory phases, which commonly occur clustered (Figure 4D). All of these accessory phases also occur locally as inclusions within albite, biotite, and orthoamphibole.

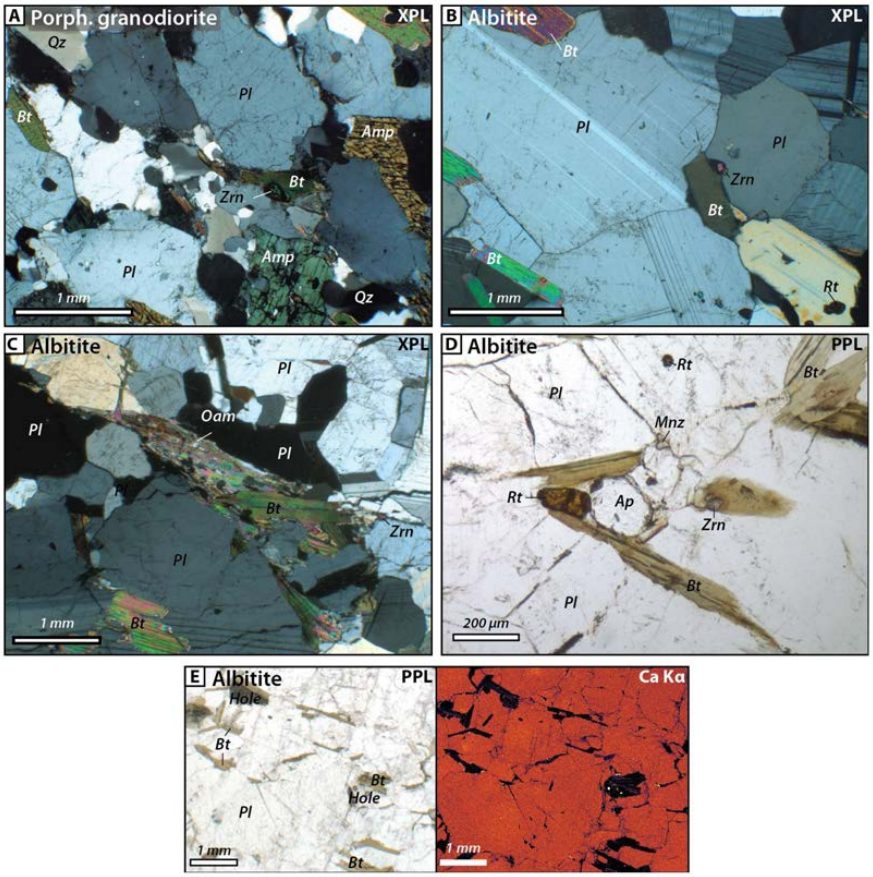

Figure 4. (**A**) Cross polarized (XPL) photomicrograph of porphyroclastic granodiorite igneous texture; (**B**) XPL photomicrograph of albitic plagioclase, biotite, and accessory minerals with albitite lens; (**C**) XPL photomicrograph of typical albitite texture and mineralogy, including orthoamphibole, biotite, plagioclase, and apatite grains; (**D**) Plane polarized (PPL) photomicrograph of typical accessory mineral phase cluster including rutile, apatite, monazite and zircon bounded by biotite along two sides; (**E**) PPL photomicrograph and Ca Kα WDS map of the same area showing flat zoning in Ca within albite.

3.3. Bulk Rock Composition

Bulk rock major and trace element compositions of the albitite, porphyroclastic granodiorite, Bear Basin schist, biotite ± garnet gneiss, and leucogranite sheets were acquired using X-ray fluorescence (XRF) analysis and can be found in Table 2. Rare earth element (REE) plots of bulk compositions for these major rock types are shown in Figure 5. The REE plots are normalized to

chondrite values from [39], and show similar patterns for the albitite and the granodiorite samples, with general enrichment in all the REEs, and slightly more enrichment in light rare earth elements (LREE) than heavy rare earth elements (HREE). The Bear Basin schist and biotite ± garnet gneiss generally have lower LREE content and similar HREE content to the albitite and the granodiorite. Leucogranite sheet samples both show negative Eu anomalies and lower LREE and lower to similar HREE than the other lithologies examined.

Table 1. Feldspar and orthoamphibole mineral compositions.

	Feldspar										Orthoamphibole		
Point	1	2	3	1 of 7	2 of 7	3 of 7	4 of 7	5 of 7	6 of 7	7 of 7	1-Ath	2-Ath	4-Ath
SiO_2	64.75	66.27	66.34	65.98	66.25	65.88	66.50	66.56	66.52	66.59	56.51	56.04	55.43
TiO_2	n.m.	n.m.	n.m.	n.m.	n.m.	n.m.	n.m.	n.m.	n.m.	n.m.	0.00	0.00	0.05
Al_2O_3	20.67	20.68	20.61	19.64	19.83	19.46	20.05	20.32	20.47	20.02	1.09	1.33	1.61
FeO	0.03	0.02	0.01	0.06	0.03	0.00	0.03	0.03	0.01	0.04	14.35	14.34	14.24
MgO	0.00	0.00	0.00	0.00	0.00	0.00	0.00	0.00	0.00	0.00	23.98	24.05	23.89
MnO	0.00	0.00	0.00	0.01	0.00	0.00	0.01	0.01	0.00	0.00	0.58	0.60	0.67
CaO	1.13	1.20	1.17	1.14	1.14	1.13	1.21	1.31	1.24	0.64	0.14	0.13	0.12
Na_2O	10.76	10.89	11.00	10.94	10.90	10.77	10.71	10.79	10.77	11.12	0.07	0.12	0.17
K_2O	0.10	0.04	0.04	0.04	0.04	0.04	0.03	0.05	0.03	0.01	0.00	0.00	0.00
H_2O	-	-	-	-	-	-	-	-	-	-	2.13	2.13	2.11
Total	97.45	99.09	99.17	97.81	98.18	97.29	98.55	99.07	99.05	98.43	98.86	98.74	98.30
An	0.05	0.06	0.06	0.06	0.06	0.05	0.06	0.06	0.06	0.06			
Ab	0.94	0.94	0.94	0.94	0.94	0.94	0.94	0.93	0.94	0.94			
Or	0.01	0.00	0.00	0.00	0.00	0.01	0.00	0.01	0.00	0.00			
Si p.f.u.*											7.95	7.90	7.86
Mg#											0.75	0.75	0.75

n.m. = not measured; p.f.u.* = Per formula unit; Mg# = (Fe + Mg)/Mg.

Table 2. Major and trace element bulk rock data.

	Albitites				Porph. Grano.	Bt ± Grt Gneiss	Bear Basin Schist	Leucogranites	
Major Elements (wt %)									
Sample	13c-10a	13c-10d	13c-10e	13c-10f	13c-10c	15c-21a	8KRB-7c	11C-06a	KM13-27
SiO_2	63.2	63.09	66.80	63.65	65.45	57.62	73.69	71.81	77.07
TiO_2	0.54	0.48	0.51	0.52	0.55	0.26	0.31	0.1	bdl
Al_2O_3	19.29	18.91	18.66	19.36	16.66	12.08	13.41	16.63	13.69
Fe_2O_3	1.38	1.61	0.69	1.30	3.70	23.50	3.9	1.32	1.15
MgO	2.33	3.31	1.24	2.22	1.47	3.98	2.62	0.55	0.07
MnO	0.02	0.02	0.00	0.02	0.03	0.18	0.07	0.02	0.06
CaO	1.39	1.05	1.16	1.24	3.57	0.37	0.54	1.45	1.06
Na_2O	9.23	9.24	9.37	9.56	5.61	1.19	3.11	4.02	6
K_2O	0.57	0.79	0.42	0.44	1.14	0.69	1.49	2.65	0.71
LOI	1.5	1.1	0.7	1.2	1.2	-0.1	0.5	1.2	0.1
Total	99.81	99.86	99.89	99.84	99.72	99.86	99.79	99.82	99.94
Trace elements (ppm)									
Ba	109	106	77	72	732	341	870	839	7
Be	3	bdl	3	2	bdl	3	1	bdl	2
Co	3.8	4.8	1.4	3.2	6.6	14.9	12.6	2	0.5
Cs	1	1.5	0.5	0.7	0.5	0.8	0.7	0.8	0.3
Ga	16.8	17.3	14.8	16.4	17.6	13.8	15.7	18.7	20.7
Hf	5.2	5.2	5.9	6.0	5.0	2.0	3.8	1.4	1.1
Nb	10.3	7.7	9.4	9.7	9.1	6.3	6.1	2.4	5.1
Rb	11	17.8	7.3	8.2	23.1	19.1	40.5	57.5	21.6
Sn	2	2	1	2	2	bdl	1	bdl	bdl
Sr	254.5	181.4	222.3	212.3	726.2	33.3	118.4	230.9	16
Ta	0.9	0.7	0.9	1.0	0.6	0.6	0.5	bdl	0.3
Th	18.1	11.2	14.8	17.0	17.2	9.5	16.4	1.2	7.3
U	2.8	1.3	2.0	3.1	2.4	5.7	4.5	0.5	2.7
V	53	56	22	38	50	71	42	16	11
W	8.4	4.6	1.5	7.1	bdl	bdl	bdl	bdl	bdl
Zr	209	202.6	238.5	237.8	214.0	77.5	125.4	45.4	18.5
Y	31.6	16.9	18.1	19.7	14.7	16.5	13.2	5.1	19.6
La	124.5	59.7	58.4	119.2	114.2	21.1	35.8	8.6	5

Table 2. *Cont.*

	Albitites				Porph. Grano.	Bt ± Grt Gneiss	Bear Basin Schist	Leucogranites	
Ce	243.2	109.7	114.8	230.1	221.3	33.5	63.5	15.1	9.4
Pr	26.68	12.82	13.50	28.08	25.93	3.87	6.35	1.62	1.03
Nd	91.8	46.6	48.5	103.6	95.8	13.6	20.9	6	3.2
Sm	14.37	7.21	7.17	15.49	12.34	2.41	3.26	0.89	1.14
Eu	2.78	1.64	1.44	2.69	2.24	0.62	0.65	0.27	0.04
Gd	9.31	5.12	5.04	9.56	7.61	2.54	2.75	0.86	1.45
Tb	1.12	0.60	0.65	0.95	0.78	0.46	0.40	0.14	0.36
Dy	5.68	3.15	3.42	4.28	3.51	2.67	2.23	0.86	2.62
Ho	0.96	0.58	0.62	0.64	0.49	0.50	0.45	0.16	0.57
Er	2.89	1.89	1.67	1.62	1.34	1.38	1.37	0.49	2.08
Tm	0.41	0.27	0.23	0.26	0.19	0.22	0.21	0.08	0.39
Yb	2.64	1.91	1.53	1.56	1.18	1.31	1.43	0.47	3.02
Lu	0.37	0.27	0.21	0.21	0.14	0.21	0.23	0.07	0.45

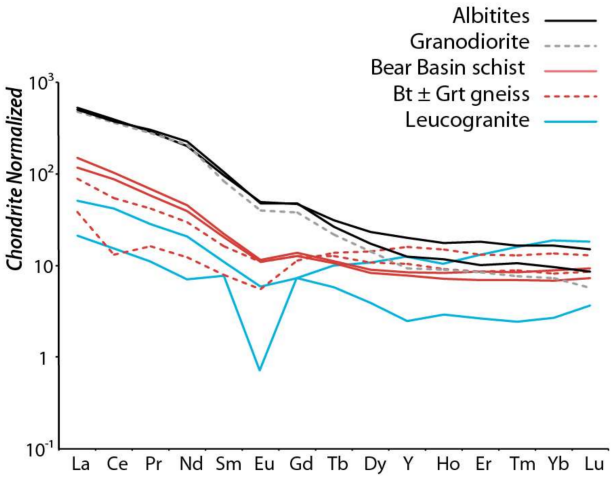

Figure 5. Rare earth element (REE) spectra for albitite, Bear Basin schist, Bt ± Grt gneiss, leucogranite sheets, and granodiorite bulk rock trace element data. Chondrite normalization uses the CI chondrite from McDonough and Sun, 1995 [39].

4. Monazite Morphology, Geochronology, and Geochemistry

Dating of zircon and monazite was conducted to understand the timing of crystallization, metamorphism, fluid flow, and metasomatism in the albitite. This work was done predominately in situ, in order to preserve the petrologic context of these phases.

The accessory mineral grains analyzed are commonly chemically zoned, with compositional domains <20 μm thick. For this reason, zircon and monazite grains were imaged before dating, to understand the full spectrum of intragrain domains and compositions. These images also allowed morphological characterization of the accessory minerals. In the case of zircon, morphology was used to understand potential alteration relationships between the albite and the other orthogneiss units within Bear Basin. Grains in all lithologies were identified in thin section by elemental full thin section maps (Y, Al, Zr, Ce, ± P) made on the JEOL 8600 and the JEOL 8230 EMPs at the University of Colorado Boulder. For full section maps, the current was set to 180 nA, acceleration voltage to 15 kV, and beam size to 25–35 μm.

4.1. Monazite Analytical Methods

After monazite grains were identified by WDS full thin section maps, which were registered to full thin section photomicrographs (Figure A1A–D), they were investigated optically to constrain context and textural occurrence. Selected grains encompassing the range of sizes, textural occurrences, and morphologies were targeted for compositional WDS U Mβ, Th Mα, Y Lα, and Si Kα maps collected

on the JEOL 8600 EMP at the University of Colorado Boulder. These maps were used to identify compositional variation across the monazite grains, and as guides for quantitative analysis. Backscatter electron (BSE) images were also taken at grain and textural setting scales.

U-Th-total Pb monazite dates and trace element compositions were acquired with the modified Cameca SX-100 (Ultrachron) EMP at the University of Massachusetts Amherst Electron Microprobe and SEM Facility. The details of analytical procedures, including count times, standards, and a list of spectrometers, follow those laid out in Appendix A of Dumond [40], Williams et al. [41], and Jercinovic [42]. Background corrections followed the multipoint background method of Allaz et al., [43]. Homogeneous chemical domains were targeted with the guidance of WDS grain maps, and a weighted mean of 3 to 6 individual spot analyses per domain was calculated and reported with a 2σ uncertainty (Table 3). This uncertainty is the larger of either the propagated analytical uncertainty of trace element compositions through the age equation plus an estimated 1% uncertainty on background intensities [41], or two times the standard error of the mean. Individual point analyses were rejected and excluded from the domain weighted mean calculation if they were inadvertently collected from a compositional domain outside the targeted area. The monazite consistency reference material used is the Moacyr Brazilian pegmatite monazite with weighted mean ID-TIMS ages of 506.4 ± 1.0 Ma (2σ, MSWD = 0.6) for $^{208}Pb/^{232}Th$, 506.7 ± 0.8 Ma (MSWD = 0.83) for $^{207}Pb/^{235}U$, and 515.2 ± 0.6 Ma (MSWD = 0.36) for $^{206}Pb/^{238}U$ [44].

Table 3. Monazite EMP U-Th total-Pb data.

Grain	Date Analyzed *	Text. Setting	Domain	Trace Element Concentrations (ppm)								N(n)†	Date (Ma)	2σ (Ma)
				Y	2σ	U	2σ	Th	2σ	Pb	2σ			
Cores														
m3	12/22/14	g.b. Bt/Pl	Core	12612	1344	1930	402	54727	17792	5086	1606	5(5)	1773	58
m12	12/22/13	g.b. Pl/Zrn/Rt	Core	11733	1898	2094	134	17645	3380	2037	174	5(5)	1735	106
m93a	12/22/14	Ap	Core	10163	1398	2000	492	2862	1250	822	220	5(5)	1743	31
m113	12/22/14	Pl	Core	8585	1004	1397	736	4113	3822	719	482	5(5)	1685	90
m124	12/22/14	Oam	Core	12642	688	1513	142	8997	990	1210	148	5(5)	1792	66
												Wt. Mean:	1750	23
													MSWD:1.15	
Rims/Whole														
m3	12/22/14	g.b. Bt/Pl	Rim	7921	890	2660	182	25424	1694	2858	138	5(5)	1754	36
m7	12/26/14	Bt	Whole	8404	590	3134	474	19846	1206	2553	138	6(6)	1758	24
m33	12/26/14	Pl	Rim	6788	658	2599	190	18976	1544	2280	146	5(5)	1729	44
m93a	12/22/14	Ap	Rim	7430	718	2550	630	15963	1682	2041	232	5(5)	1741	56
m96	12/26/14	g.b. Rt/Pl	Whole	8571	266	2801	140	18192	1142	2273	100	6(6)	1727	20
m113	12/22/14	Pl	Rim	6301	842	2505	648	18859	3608	2242	420	3(5)	1728	18
m116	12/23/14	g.b. Ap/Pl	Whole	7679	1124	2820	590	20858	1712	2486	230	6(6)	1723	26
m124	12/22/14	Oam	Rim	7363	1264	2770	242	19977	1538	2405	204	6(6)	1725	38
												Wt. Mean:	1734	10
													MSWD:1.03	
Consistency Standard														
	12/22/14			11090	142	933	58	60831	222	1455	56	4(4)	507	19
	12/22/14			11030	106	1189	144	61157	460	1482	64	6(6)	507	22
	12/23/14			11343	174	967	80	60935	216	1443	36	6(6)	501	12
	12/23/14			11412	176	932	94	60912	236	1449	32	6(6)	504	16
	12/26/14			11336	236	993	100	61050	276	1456	18	6(6)	504	6
	12/26/14			11176	144	932	122	60794	376	1434	32	6(6)	500	10
												Wt. Mean:	503	4
													MSWD:0.18	

* Dates are month/day/year; †N is number of points used for domain date, n is total number acquired; g.b., Grain Boundary. Wt. mean, weighted mean.

4.2. Monazite Size, Morphology, Textural Context, and Compositional Zoning

Monazite grains range in size from 35 μm to 200 μm in length. The majority of grains are anhedral to subhedral, and rounded or irregularly shaped. Several grains are elongate and form multi-grain trains (Figure 6A). Monazite occur as single grains included in orthoamphibole (Figure 6B), biotite (Figure 6A), and feldspar (Figure 6C; Table 3), and as clusters of grains associated with apatite, rutile or zircon (Figure 6D,E).

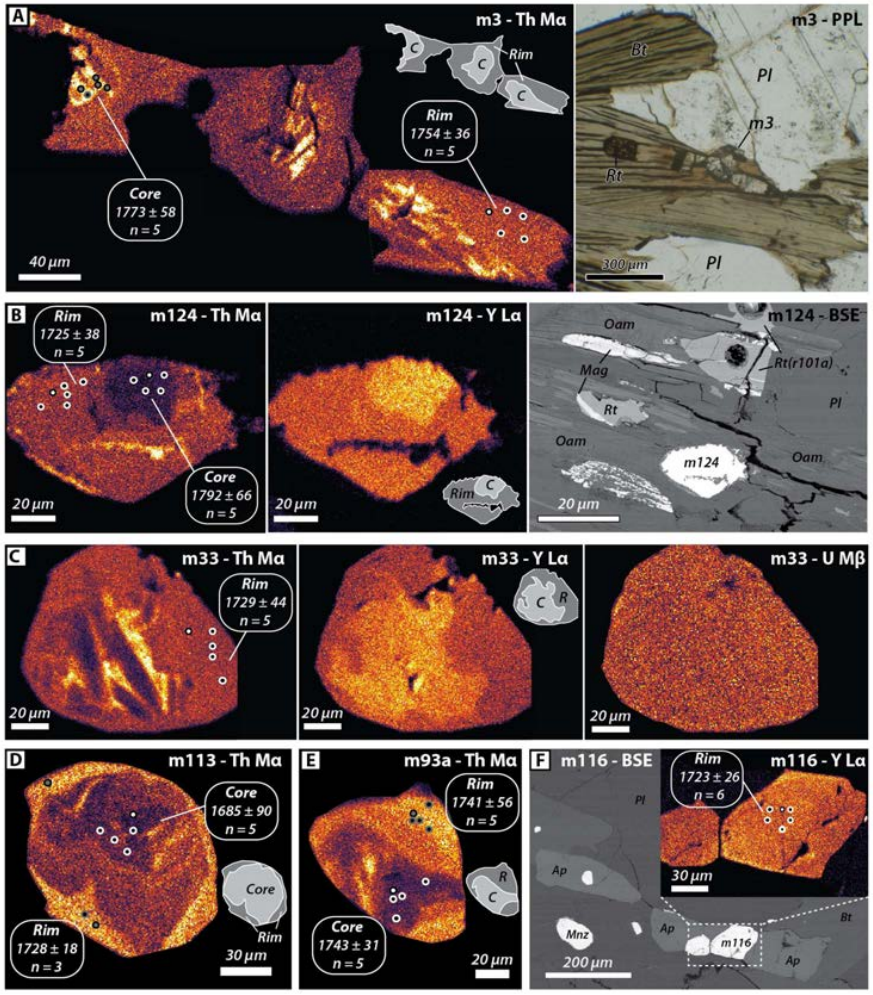

Figure 6. Monazite morphology, textural context, and compositional zoning shown in WDS maps, plane polarized light (PPL), and BSE imagery from albitite sample 13c-10a. Calculated EMP U-Th-total Pb dates (Ma) are based on the locations of each individual EMP analyses, which are shown as circles on each dated monazite domain. Sketches of domain identifications placed where applicable. C annotates monazite core domains, R annotates monazite rim or whole domains. (**A**) Th Mα WDS map and PPL photomicrograph of monazite grain m3; (**B**) Th Mα and Y Lα WDS maps and BSE textural image of monazite grain m124; (**C**) Th Mα, Y Lα WDS map of m33; (**D**) Th Mα WDS map of m113; (**E**) Th Mα WDS map of m93a; (**F**) Y Lα WDS map and BSE images of m116.

Two distinct monazite textural ± compositional domains occur in this sample, commonly within the same grains (Figure 6A–E). Core domains occur only as internal cores within multidomainal grains, and contain relatively high and uniform Y, uniform and relatively low U (<2100 ppm), and irregularly zoned Th (e.g., Figure 6A), with overall relatively low concentrations down to 0.2 wt %, but with patches as high as 5.5 wt % (Table 3, e.g., Figure 6E). Rim domains consist of either whole grains (Figure 6E) or rims surrounding core domains (Figure 6A–C). These domains contain higher U (>2100 ppm), more uniform and generally higher Th (1.5 wt % < Th < 3.5 wt %), and lower Y than cores (Table 3). In the same grains, the two domains are visually discernable in WDS maps by these compositional differences and jagged boundaries between them, interpreted as resorption (Figure 4B,C).

4.3. Monazite U-Th Total Pb Results

A total of 26 grains were imaged via WDS maps, and nine grains were dated by EMP U-Th-total Pb. Four of these grains contain multiple age domains (with distinct cores and rims), for a total of 13 domains

dated within this sample (Figure 7A, Table 3). Of the dated domains, five were high Y cores, and eight were from high Th, low Y rims or whole grains. The oldest two dates are core domains from a grain included in orthoamphibole (1792 ± 66 Ma, 2σ, n = 5, m124 core) and a monazite along a Bt-Ab grain boundary (1773 ± 58 Ma, 2σ, n = 5, m3 core). The youngest date is also from a core domain of a grain included within albite (1685 ± 90 Ma, 2σ, n = 5, m113 core), which has the second largest uncertainty of any domain. The five core domains have a weighted mean of 1750 ± 23 Ma (2σ, n = 5, MSWD = 1.15). The remaining eight analyses are all rims or whole grains, and range from 1758 ± 24 Ma (2σ, n = 6, m7) to 1723 ± 26 Ma (2σ, n = 6, m116). These have weighted means of 1734 ± 10 Ma (2σ, n = 8, MSWD = 1.03). The Moacyr consistency reference monazite analyzed during these data acquisition sessions has a weighted mean age of 503 ± 4 Ma (2σ, n = 6, MSWD = 0.18, Table 3).

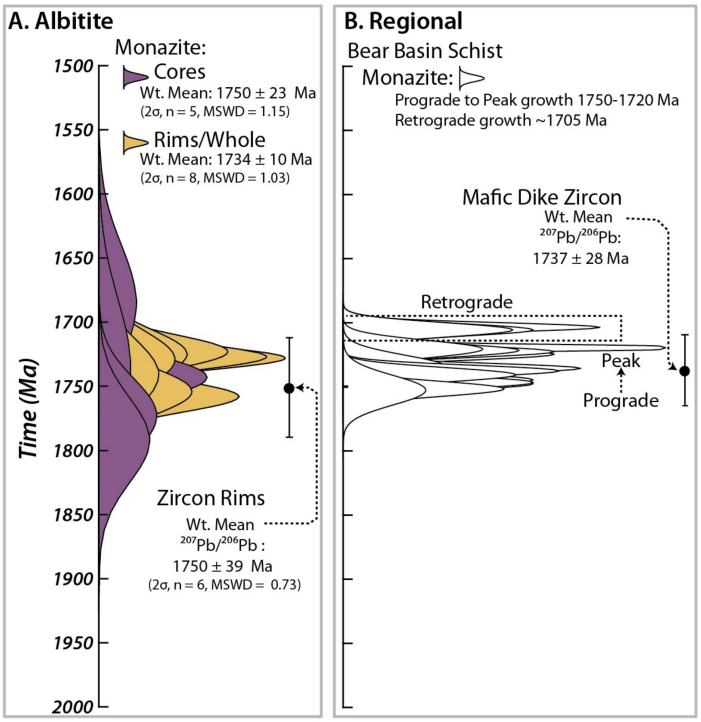

Figure 7. Gaussian normalized histograms of Monazite EMP U-Th-total Pb data and timing of zircon geochronology. (**A**) Monazite results for this study. Each histogram curve is the calculated weighted date for a single domain composed of multiple individual EMP data acquisition points (see Table 2). Zircon rims $^{207}Pb/^{206}Pb$ weighted mean age also shown; (**B**) Monazite and zircon geochronologic data from the Bear Basin schist and a deformed mafic dike from the Gallatin Peak terrane [20].

4.4. Monazite Geochemistry

Complete element compositions of monazite were collected simultaneously with the acquisition of U-Th-total Pb data. Compositional data are shown in Table 4, and plots of REE data normalized to (1) chondrite values and (2) the mean of monazite rim domains are shown in Figure 8A. The chondrite normalized plots show that both core and rim domains are enriched in LREE, have minor negative Eu/Eu* anomalies from 0.38 to 0.73 (both domains have a mean Eu/Eu* of ~0.6), and are depleted in HREE. There is a positive Tm anomaly that may be due to an underestimation in the background correction [45]. It is difficult to see any difference in REE patterns between different monazite domains when each is normalized to chondrite values, but core domains show higher enrichment in MREE and HREE than rims when normalized to the mean of monazite rim domains (Figure 8A). Apparent breaks in the data are where the concentration was below detection.

Table 4. Monazite REE data.

Element (ppm)	Monazite Cores			
	m3 core	m93a core	m113 core	m124 core
La	119,068	141,130	149,867	113,933
Ce	238,550	275,997	280,911	254,699
Pr	25,832	28,662	27,915	31,054
Nd	96,513	105,262	98,427	130,413
Sm	7904	7036	5095	10,652
Eu	1656	1559	1508	1323
Gd	8852	8129	6737	10,762
Tb	468	436	-	-
Dy	3146	2381	2026	3231
Y	12,684	10,150	8573	12,656
Ho	-	-	-	-
Er	777	759	710	948
Tm	834	904	576	895
Yb	-	-	-	-

Element (ppm)	Monazite Rims								
	m3 rim	m93a rim	m113 rim	m124 rim	m12	m116	m7	m96	m33
La	136,363	144,043	143,050	139,348	138,438	139,458	136,420	136,288	140,532
Ce	263,718	274,811	272,628	269,086	266,595	270,552	266,161	269,439	272,556
Pr	27,414	27,187	27,415	27,286	27,149	27,499	27,674	27,737	27,580
Nd	97,694	96,188	97,102	98,831	99,080	100,171	101,508	102,750	100,543
Sm	5615	5154	4346	5103	6898	5282	6026	5966	5402
Eu	933	1408	1117	999	1699	1066	1120	1418	1094
Gd	6650	5943	5206	5530	7236	6098	6724	6970	6208
Tb	-	-	-	-	332	-	-	247	311
Dy	1799	1602	1098	1504	2705	1786	1875	1736	1590
Y	7943	7444	6315	7380	11,659	7697	8423	8589	6803
Ho	-	-	-	-	-	-	-	-	-
Er	498	432	656	389	919	593	549	602	548
Tm	941	853	429	464	768	738	767	704	874
Yb	-	-	-	-	408	-	-	-	-

"-" indicates value below detection limit of EMP or LA-ICP-MS; n/a indicates element not measured.

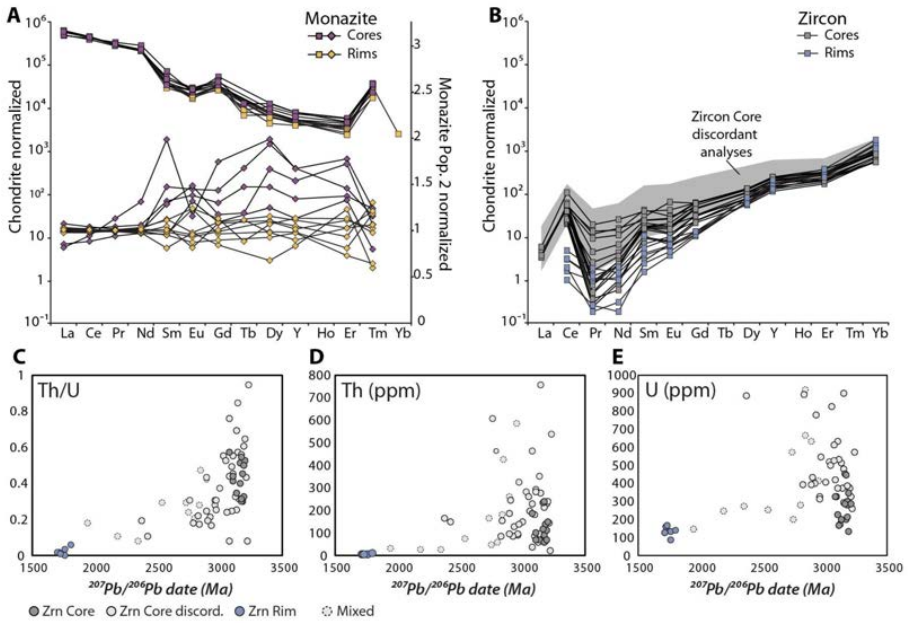

Figure 8. REE spectra for (**A**) monazite separated by domains normalized to chondrite (squares) on the left axis and to the mean of monazite rims on the right (diamonds); REE spectra for (**B**) zircon separated by domain and secondarily by discordance. Chondrite normalizations use the CI chondrite from [39]; (**C**) Zircon Th/U vs ^{207}Pb-^{206}Pb date color coded by domain; (**D**) Zircon Th content in ppm vs ^{207}Pb-^{206}Pb date color coded by domain; (**E**) Zircon U content in ppm vs ^{207}Pb-^{206}Pb date color coded by domain.

5. Zircon Morphology, Geochronology, and Geochemistry

5.1. Zircon Analytical Methods

Zircon grains were characterized for the albitite, porphyroclastic granodiorite, hornblende monzodiorite, and biotite-garnet gneiss. These grains were identified by full section EMP maps registered to full thin section photomicrographs (Figure A1), investigated optically on a transmitted light microscope, and then selected for microbeam imaging based on representations of the full suite of textural settings and morphologies. For albitite sample 13c-10a cathodoluminescence (CL), BSE and secondary electron (SE) images were taken on the JEOL 6610 LV Scanning electron microscope at the University of Northern Colorado, whereas all other samples were imaged (CL and BSE) on the JEOL 8230 EMP at the University of Colorado Boulder.

A suite of zircon was targeted for in situ trace element and geochronological analyses in thin sections that encompassed the full range of compositions and morphologies. A second suite of grains from sample 13c-10a was separated via standard crushing methods and concentrated in the <250 μm fraction. This fraction was then hand washed to minimize potential loss of small (<20 μm) zircon, magnetically separated, and run through heavy liquids. Grains were then picked and placed on double-sided tape to enable depth profiling on the laser ablation inductively coupled plasma mass spectrometer (LA-ICP-MS). After analysis, these grains were imaged in plane polarized light.

Zircon within the albite sample 13c-10a were dated in situ and as separates via U-Pb by LA-ICP-MS at the University of Kansas, with an Element2 ICP-MS coupled with a Photon Machines Analyte.G2 193 nm ArF excimer laser. A spot size of 15 μm was used for analyses in order to resolve potentially small-scale internal zonation. U-Pb and trace element data were collected within the same pit during a single acquisition. The primary U-Pb reference material used was GJ1 with a TIMS $^{207}Pb/^{206}Pb$ age of 608.53 ± 0.37 Ma [46]. The trace element primary reference material was NIST612 [47]. Plešovice zircon was used as a secondary reference material for U-Pb dating, which has a ID-TIMS U-Pb age of 337.13 ± 0.37 Ma (2σ, [48]). Elemental fractionation, down-hole fractionation, and calibration drift were corrected by bracketing measurements of unknowns with the reference materials, using the IOLITE software package [49,50]. The VizualAge data reduction scheme was used for U-Pb data reduction [51].

5.2. Zircon Size, Morphology, Textural Context, and Compositional Zoning

5.2.1. Albitite Zircon

Zircon within albitite samples occur most commonly as single grains (e.g., Figure 9A,B; Figure A2), but also notably as distinct clusters of multiple grains, referred to hereafter as glomerocrysts (Figure 9C,D; Figure A2B). Zircon grains range in length from 200 μm to 20 μm (Table 5), including single grains and glomerocrysts. They are euhedral to anhedral and elongate to rounded. The glomerocrysts consist of three to ten individual grains (~20–40 μm across each) sharing rim domains of bright CL material. CL and BSE images show an internal zoning texture and multiple intragrain domains consisting of bright CL rims and dark CL cores (Figure 9A–E,G; Figure A2B). The bright CL rims are ~5–20 μm thick, do not appear compositionally zoned, and are inclusion-free in BSE images. Dark CL core domains appear to have concentric zoning typical of igneous zircon (Figure 9E; Figure A2). In some grains, this internal concentric zoning is truncated by the bright CL rim, suggesting dissolution–reprecipitation processes (Figure 9B; Figure A2). Electron backscattered diffraction (EBSD) maps of zircon glomerocrysts indicate that the individual subgrains (cores and rims) are oriented differently from one another (Figure 9C).

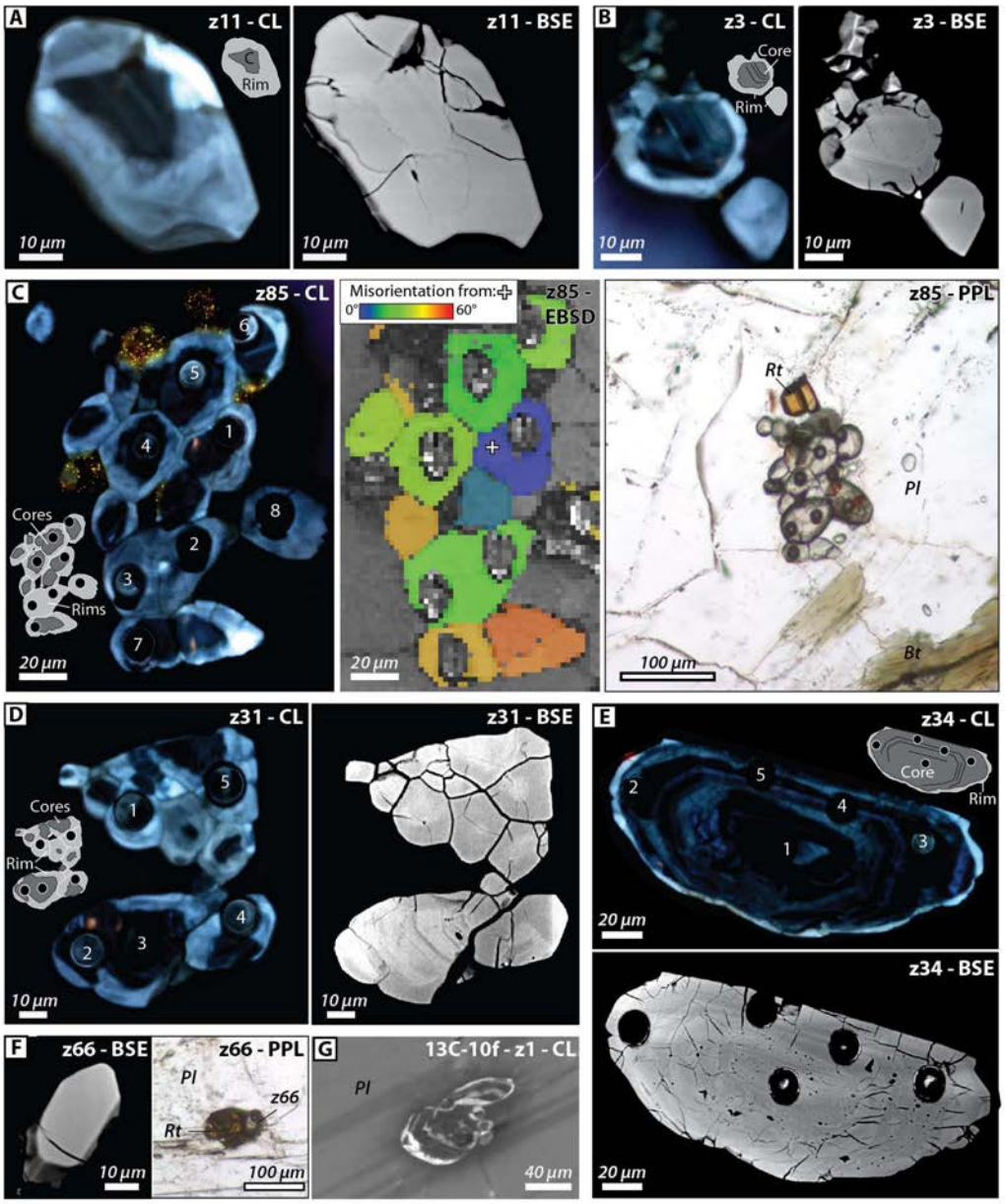

Figure 9. Zircon morphology and compositional zoning shown in CL, BSE, secondary electron (SE) and plane polarized light (PPL) photomicrographs for albitite samples 13c–10a (**A**–**F**) and 13c-10f (**G**). LA-ICP-MS analysis pits numbered where applicable. Sketches of rim and core domains shown when needed. (**A**) CL and BSE image of zircon grain z11 showing clear rim and core structure; (**B**) CL and BSE images of z3 which contains truncation of the core by bright CL rim; (**C**) CL, BSE, EBSD misorientation map, and PPL images of zircon glomerocryst z85; (**D**) CL and BSE images of zircon glomerocryst z31; (**E**) CL and BSE images of z34 showing clear oscillatory zoning within the core zone surrounded by thin bright CL rims; (**F**) BSE and PPL images of z66, a grain completely composed of bright CL material; (**G**) CL image of z1 from sample 13C-10f, a partial glomerocryst contained completely in plagioclase.

Zircon glomerocrysts and single grains occur as inclusions in plagioclase (Figure 10C,F,G) biotite, rutile, and as clusters with monazite, rutile, and apatite (Figure 10C,F; Table 5). The CL dark cores have Th-U ratios from 0.08 to 1.34, while CL bright rims have Th/U ratios < 0.05 (Table 5). Based on the consistent rim and core domain morphology and clear differences in Th/U ratios, dark CL cores are designated zircon core domains, while bright CL rims are designated zircon rim domains. While the

majority of rim domains are actually rims around core domains, several small grains (~30 µm across), comprised completely of bright CL rim material, occur locally in feldspar (Figure 9F).

5.2.2. Other Orthogneiss Zircon Morphology

Zircon morphology and zoning were imaged from the hornblende monzodiorite, biotite ± garnet gneiss, and porphyroclastic granodiorite, to directly compare to the zircon morphology and zoning in the albitite. Locations of these accessory minerals within full thin section photomicrographs can be seen in Figure A1E–G. Zircon within the hornblende monzodiorite ranges from 20 to 100 µm with complicated multi-domainal cores and thin ~10 µm bright CL rims (Figure 10A; Figure A3A). Zircon cores in this sample are not concentrically zoned. The zircon within the biotite ± garnet gneiss are 20–40 µm across, and have a wide range of textures from concentrically zoned grains to complicated patchy grains (Figure 10B,C; Figure A3B). There are no bright CL rims around any of the zircon in this rock type. Zircon from the porphyroclastic granodiorite are 15–60 µm across, and concentrically zoned (Figure 10D; Figure A3B) and lack bright CL rims. No zircon glomerocrysts were observed in any of these units.

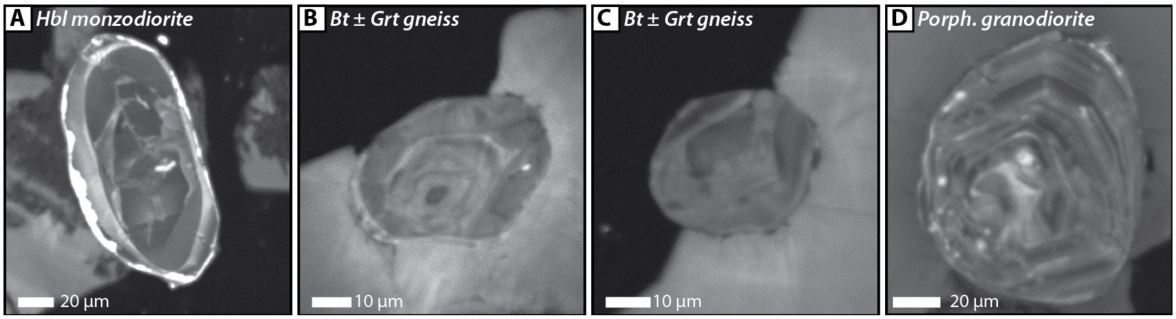

Figure 10. CL images of zircon from major units in the Bear Basin region. (**A**) Hornblende monzodiorite; (**B**) and (**C**) Bt ± Grt gneiss; (**D**) Porphyroclastic granodiorite.

5.3. Zircon U-Pb Results

A total of 22 zircon grains were analyzed in situ, while 7 were analyzed as separate from albitite sample 13c-10a. Data from a total of 67 spots with a diameter of 15 µm (e.g. Figure 9C–E) were collected (Table 5). Of the 22 grains analyzed in thin section, seven are included in feldspar, 2 grains are included in biotite, and the remaining grains occur along grain boundaries.

Using the LA-ICP-MS technique for complicated multidomain grains is powerful, not only because of the small spatial resolution of the laser beam, but also because of the time (depth) dependent data collected for each laser pit. Thus, it is possible to depth profile and observe chemical and age domains in the z-direction. Several pits drilled through rim domains into cores (e.g., s z1 spot 1a and 1b, Table 5) and the data allow separating different age domains within a single pit. However, some of the depth profiles represent mixes of both rim and core domains (Table 5), where the pit was not perpendicular to the contact between the domains.

A total of seven analyses of rim domains have $^{207}Pb/^{206}Pb$ dates ranging from 1722 ± 69 Ma (2σ, z76 spot 1) to 1958 ± 99 Ma (2σ, z31 spot 5). Six of these analyses are concordant at 1σ (Figure 11), and yield a $^{207}Pb/^{206}Pb$ weighted mean date of 1750 ± 39 Ma (2σ, MSWD = 0.70).

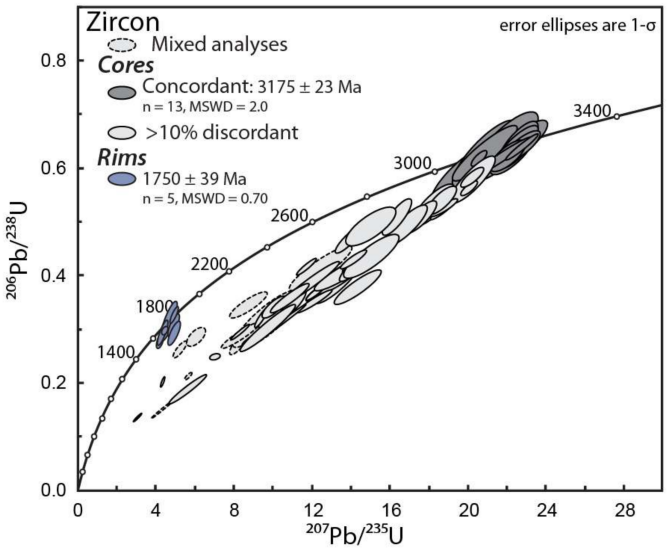

Figure 11. Concordia diagram showing U-Pb data from zircon from albitite sample 13c-10a. Ellipses are separated by domain designation of the analysis. Weighted mean $^{207}Pb/^{206}Pb$ dates based on concordant analyses from each domain are labeled in the top left corner.

The other 60 analyses are either mixed spots (the pit straddled the boundary between core and rim zircon material, n = 9) or are completely within zircon cores (n = 51). The majority of these analyses are highly discordant (Figure 9, up to ~66% for spots within cores and ~69% for mixed domains). The 51 analyses of core domains have $^{207}Pb/^{206}Pb$ dates ranging from 2383 ± 68 Ma (2σ, z2 spot 1) to 3243 ± 85 Ma (2σ, z16 spot 1). Of these, 13 analyses are concordant (at 1σ), and yield a $^{207}Pb/^{206}Pb$ weighted mean date of 3175 ± 23 Ma (2σ, MSWD = 2.0). The Plešovice zircon standard yielded a weighted mean ^{207}Pb-^{235}U age of 340.0 ± 3.4 Ma (2σ, MSWD = 1.6), a weighted mean ^{206}Pb-^{238}U age of 339.3 ± 2.8 Ma (2σ, MSWD = 0.61), a ^{208}Pb-^{232}Th age of 354.0 ± 10 (2σ, MSWD = 1.4), and a ^{207}Pb-^{206}Pb age of 330 ± 18 (2σ, MSWD = 0.91).

5.4. Zircon Trace Element and Thermometry Results

Each zircon laser spot has U-Pb and trace element data from the same aliquot of material. REE data are shown in Table 6, and as chondrite normalized spectra in Figure 8B. Generally, core domain zircon is enriched in HREE and depleted in LREE, with a marked Ce anomaly (Ce/Ce* ranging from 6.75–10.21), and little to no Eu anomaly. Rim domain zircon are more depleted in the LREE, and have a steeper slope and slightly enriched HREE relative to core domains. La content was too low to measure in the rims (detection limit ~0.2 ppm), and in many of the zircon in the core domains. There is a stark difference in Th, U, and Th–U ratios between the two zircon domains. Concordant cores have a mean Th/U of 0.42 ± 0.10, Th mean content of 119 ± 61 ppm, and U mean content of 271 ± 95 ppm (uncertainty at 1σ; Table 5; Figure 8C–E). Rim zircon have a mean Th/U of 0.021 ± 0.017, very low mean Th content of 3 ± 2 ppm, and mean U content of 129 ± 28 ppm (uncertainty at 1σ; Table 5; Figure 8C–E).

Table 5. Zircon U-Pb LA-ICP-MS data.

	Long Axis	Sidhort Axis													Dates (Ma)					%
Grain	**(μm)**	**(μm)**	**Spot**	**Domain**	**$^{207}Pb/^{235}U$**	**2σ**	**$^{206}Pb/^{238}U$**	**2σ**	**$^{207}Pb/^{206}Pb$**	**2σ**	**Th (ppm)**	**U (ppm)**	**Th/U**	**$^{206}Pb/^{238}U$**	**2σ**	**$^{207}Pb/^{235}U$**	**2σ**	**$^{207}Pb/^{206}Pb$**	**2σ**	**disco.**
z17	110	70	1	Core	22.5	1.4	0.645	0.057	0.254	0.015	57	194	0.29	3210	230	3212	60	3181	90	-2.6
z8	40	30	2	Core	21.8	2.3	0.642	0.084	0.249	0.021	67	196	0.34	3120	320	3120	110	3140	130	-2
z21	60	45	3	Core	20.8	2.2	0.63	0.068	0.235	0.012	182	323	0.56	3120	270	3122	96	3088	83	-1.6
s* z17	40	25	1	Core	22.9	1.5	0.656	0.047	0.25	0.011	132	296	0.45	3240	180	3213	62	3191	72	-1.5
z8	40	30	1	Core	20.8	2.2	0.627	0.084	0.246	0.02	66	161	0.41	3080	330	3090	110	3120	120	-1
z17	110	70	4	Core	22.4	1.5	0.639	0.056	0.255	0.013	62	209	0.30	3180	220	3191	71	3192	78	-0.9
s z21	100	55	1	Core	20.52	0.55	0.62	0.02	0.239	0.0055	97	223	0.43	3108	78	3115	26	3111	37	-0.2
z88	60	50	1	Core	22.7	1.3	0.642	0.039	0.2515	0.0087	84	271	0.31	3180	150	3204	54	3186	54	-0.1
s z26	120	100	1	Core	22.7	1.1	0.641	0.031	0.2524	0.0042	110	340	0.32	3180	130	3206	52	3198	26	0.3
z21	60	45	2	Core	22	1.2	0.625	0.038	0.248	0.011	229	450	0.51	3110	150	3170	53	3171	64	0.9
s z16	100	50	1	Core	22.2	1.5	0.628	0.051	0.257	0.014	147	281	0.52	3130	200	3184	64	3215	85	2
z20	70	45	3	Core	21.7	2	0.622	0.049	0.2525	0.0056	65	131	0.50	3110	200	3188	79	3199	37	2.3
s z18	100	60	1	Core	20.17	0.75	0.584	0.024	0.2492	0.0071	111	283	0.39	2958	99	3093	35	3172	45	5.7
z9	45	40	2	Core	19.4	1.8	0.582	0.068	0.252	0.016	236	438	0.54	2900	280	3052	96	3180	100	7
z53	45	45	2	Core	20.2	1.5	0.582	0.058	0.258	0.015	138	324	0.43	2910	230	3076	71	3220	94	7.5
s z17	40	25	2	Core	20.01	0.54	0.564	0.017	0.2529	0.0056	225	377	0.60	2880	71	3090	26	3200	35	10
z17	110	70	2	Core	15	1.7	0.493	0.048	0.218	0.015	88	324	0.27	2550	210	2820	110	2970	130	10.7
z16	40	30	2	Core	18.2	1.4	0.533	0.051	0.246	0.013	347	507	0.68	2730	210	3007	73	3143	82	10.8
z21	60	45	1	Core	16.3	1	0.51	0.045	0.23	0.012	280	513	0.55	2630	190	2901	62	3042	85	11.1
z54	80	70	2	Core	18.6	1	0.542	0.035	0.2482	0.0091	88	286	0.31	2780	150	3029	49	3162	58	13
s z1	100	50	1b	Core	18.73	0.94	0.528	0.022	0.2543	0.0065	233	364	0.64	2728	91	3021	50	3208	41	15.4
z59	40	30	4	Core	17.5	1.1	0.511	0.039	0.249	0.013	270	476	0.57	2640	170	2947	61	3157	77	16
z34	200	80	5	Core	18.72	0.88	0.525	0.026	0.2577	0.0049	20	254	0.08	2720	110	3024	44	3231	30	16.1
z54	80	70	1	Core	13.83	0.91	0.469	0.034	0.2203	0.0077	94	310	0.30	2460	150	2729	62	2972	56	16.2
z54	80	70	3	Core	16.8	1.4	0.495	0.05	0.246	0.014	91	367	0.25	2560	210	2896	88	3147	89	16.5
z89L	50	30	1	Core	16.35	0.79	0.478	0.02	0.2464	0.0051	750	890	0.84	2514	89	2904	48	3158	33	19.6
z2	70	60	4	Core	11.69	0.67	0.418	0.021	0.2014	0.0046	82	386	0.21	2246	94	2566	55	2833	37	20.7
z85	150	50	6	Core	14.1	0.87	0.432	0.023	0.225	0.0064	147	401	0.37	2310	110	2766	51	3014	45	20.9
z9	45	40	1	Core	15	1.9	0.438	0.054	0.242	0.017	177	365	0.48	2350	250	2790	120	3110	110	23.3
z85	150	50	2	Core	13.94	0.54	0.424	0.023	0.2423	0.0077	54	166	0.32	2280	100	2752	41	3131	50	26.7
z59	40	30	3	Core	14.4	1.4	0.426	0.046	0.24	0.011	289	530	0.55	2300	210	2761	87	3120	74	27.1
z20	70	45	1	Core	13.5	1.9	0.406	0.042	0.2209	0.0082	323	1086	0.30	2190	190	2690	130	2983	60	27.3
s z24	60	60	1	Core	13.4	1.7	0.401	0.045	0.235	0.012	32	416	0.08	2200	220	2700	120	3088	74	27.7
z85	150	50	5	Core	11.9	1.9	0.389	0.052	0.214	0.01	82	393	0.21	2070	240	2520	170	2929	78	30
z59	40	30	1	Core	13.2	1.4	0.385	0.045	0.237	0.013	280	624	0.45	2160	230	2660	100	3114	95	30.9
z85	150	50	4	Core	10.8	1.3	0.36	0.035	0.2069	0.0069	92	385	0.24	1990	170	2470	110	2903	56	33.4
z31	60	60	3	Core	10.01	0.83	0.343	0.027	0.211	0.011	183	429	0.43	1890	130	2419	76	2905	81	34.1
s z1	100	50	2	Rim	12.18	0.72	0.371	0.021	0.2356	0.0049	225	517	0.44	2025	99	2602	55	3086	33	34.6
z19	70	45	1	Core	12.18	0.68	0.369	0.02	0.2364	0.0073	79	324	0.24	2039	92	2619	50	3107	48	34.6
z16	40	30	1	Core	14.3	1.6	0.38	0.043	0.256	0.014	535	569	0.94	2050	200	2720	110	3243	85	35.8
z53	45	45	1	Core	10.96	0.88	0.349	0.034	0.236	0.014	257	494	0.52	1910	160	2491	76	3058	97	36.1
s z1	100	50	3	Core	12.52	0.46	0.367	0.016	0.251	0.0058	210	379	0.55	2012	77	2646	37	3187	37	37.4
z19	70	45	2	Core	12.1	1.2	0.354	0.029	0.2352	0.0057	461	610	0.76	1940	140	2574	90	3083	39	37.5
z34	200	80	2	Core	9.39	0.46	0.324	0.024	0.2154	0.0057	124	770	0.16	1800	120	2383	48	2943	42	38.6
z2	70	60	1	Core	8.28	0.63	0.297	0.019	0.2029	0.0045	149	884	0.17	1706	99	2262	73	2845	37	40
s z26	120	100	2	Core	9.12	0.95	0.289	0.022	0.2213	0.0072	136	543	0.25	1630	110	2348	92	2980	59	42.8
z34	200	80	4	Core	10.3	1.8	0.311	0.049	0.2333	0.0061	191	820	0.23	1700	230	2330	160	3068	42	45.3
z34	200	80	3	Core	9.7	1.9	0.304	0.057	0.2134	0.0099	242	1300	0.19	1650	280	2170	230	2911	77	46.8

Table 5. *Cont.*

Grain	Long Axis (μm)	Sidhort Axis (μm)	Spot	Domain	$^{207}Pb/^{235}U$	2σ	$^{206}Pb/^{238}U$	2σ	$^{207}Pb/^{206}Pb$	2σ	Th (ppm)	U (ppm)	Th/U	Dates (Ma) $^{206}Pb/^{238}U$	2σ	$^{207}Pb/^{235}U$	2σ	$^{207}Pb/^{206}Pb$	2σ	% disco.
z20	70	45	2	Core	7	0.36	0.251	0.0086	0.195	0.011	458	2580	0.18	1443	45	2107	47	2800	100	47.1
z2	70	60	3	Core	4.31	0.17	0.205	0.013	0.1546	0.0062	163	880	0.19	1197	69	1690	32	2383	68	50.6
z34	200	80	1	Core	5.6	1.3	0.19	0.036	0.1957	0.0093	600	1980	0.30	1130	190	1760	180	2770	77	60.5
z2	70	60	2	Core	3.04	0.28	0.138	0.011	0.1591	0.0042	144	1405	0.10	829	60	1401	74	2438	45	65.8
z85	150	50	3	Rim	4.92	0.28	0.329	0.02	0.1064	0.0041	3	153	0.02	1827	98	1812	49	*1735*	*68*	-6.9
z31	60	60	4	Rim	4.62	0.56	0.317	0.049	0.111	0.01	2	82	0.03	1750	240	1750	110	*1770*	*160*	-5
z66	30	20	1	Whole	4.32	0.37	0.295	0.031	0.1097	0.0072	0	125	0.00	1650	150	1675	68	*1770*	*120*	0
z76	60	20	1	Rim	4.42	0.19	0.299	0.01	0.1059	0.0039	2	119	0.02	1683	50	1712	36	*1722*	*69*	2.8
z31	60	60	1	Rim	4.87	0.42	0.309	0.029	0.1119	0.006	7	136	0.05	1730	140	1781	74	*1813*	*95*	4
s z1	100	50	1a	Rim	4.17	0.22	0.28	0.019	0.107	0.0061	1	161	0.01	1587	96	1664	44	*1740*	*100*	10
z31	60	60	5	Rim	4.91	0.44	0.295	0.029	0.1222	0.0071	25	144	0.18	1650	140	1790	77	1958	99	16.1
z59	40	30	2	Mix	12.4	2.1	0.415	0.056	0.2	0.019	54	272	0.20	2200	250	2510	180	2810	160	20.1
z31	60	60	2	Mix	8.7	1.3	0.347	0.033	0.175	0.015	72	248	0.29	1900	160	2230	140	2550	160	22.6
z85	150	50	7	Mix	6.01	0.65	0.287	0.023	0.149	0.011	21	270	0.08	1620	110	1980	100	2360	140	28.8
z85	150	50	1	Mix	5.18	0.48	0.265	0.02	0.1363	0.0066	24	243	0.10	1510	100	1879	80	2193	81	30.5
z7	40	30	1	Mix	9.7	2.3	0.32	0.074	0.212	0.029	179	659	0.27	1750	350	2290	240	2850	200	38
z85	150	50	8	Mix	8.3	1.3	0.29	0.032	0.195	0.014	46	193	0.24	1650	170	2160	150	2760	120	40.2
z17	110	70	3	Mix	8.58	0.9	0.29	0.029	0.212	0.015	259	630	0.41	1620	140	2274	90	2900	120	42.3
z73	40	25	1	Mix	8.33	0.75	0.281	0.035	0.219	0.012	580	405	1.43	1590	170	2252	85	2959	89	46.9
z89U	50	40	1	Mix	5.63	0.26	0.2142	0.0086	0.1908	0.0055	162	567	0.29	1250	45	1913	39	2741	47	53.8
s z26	120	100	3	Mix	4.29	0.77	0.153	0.023	0.2034	0.0063	424	910	0.47	900	130	1650	150	2855	52	69

* s before grain indicates zircon separate analyses; g.b. grain boundary; Bold 207Pb/206Pb dates used for core domain weighted mean age of 3175 ± 23 (2σ, MSWD = 2.0); Bold Italic 207Pb/206Pb dates used for rim domain weight mean age of 1750 ± 39 (2σ, MSWD = 0.70).

Table 6. Zircon REE data.

Element	Rim Zircon								Core Concordant Zircon													
(ppm)	z85 3	z31 4	z66 1	z76 1	z31 1	s z1 1a	z17 1	z8 2	z21 3	s z17 4	z8 1	z17 4	s z21 1	z88 1	s z26 1	z 21 2	s z16 1	z20 3	s z18 1	z9 2	z53 2	s z17 2
La	-	-	-	-	-	-	-	-	6	3	4	-	-	-	-	-	-	4	-	-	-	-
Ce	2	2	3	1	5	3	20	26	109	57	52	22	34	24	26	51	40	47	39	63	40	57
Pr	1	0	1	0	2	1	0	3	19	12	14	0	1	0	0	1	1	9	2	1	1	5
Nd	1	0	2	0	1	1	1	4	26	16	15	1	2	1	2	3	2	11	4	3	2	7
Sm	4	2	11	2	6	4	10	17	40	25	43	9	17	3	7	17	15	30	22	18	16	24
Eu	6	4	7	5	9	6	8	19	43	27	31	8	12	7	10	17	12	66	18	21	15	26
Gd	13	11	13	11	13	11	24	31	63	63	47	24	24	22	32	47	31	62	47	55	45	61
Tb	n/a	n/a	n/a	n/a	n/a	n/a	n/a	n/a	n/a	n/a	n/a	n/a	n/a	n/a	n/a	n/a	n/a	n/a	n/a	n/a	n/a	n/a
Dy	61	67	60	83	81	66	69	78	135	130	106	69	83	57	93	111	81	126	111	127	109	135
Y	154	169	130	212	181	169	130	145	241	252	173	141	171	117	199	201	152	248	211	231	210	252
Ho	n/a	n/a	n/a	n/a	n/a	n/a	n/a	n/a	n/a	n/a	n/a	n/a	n/a	n/a	n/a	n/a	n/a	n/a	n/a	n/a	n/a	n/a
Er	292	306	248	384	309	299	191	209	304	373	223	221	245	173	294	274	204	331	296	323	295	318
Tm	n/a	n/a	n/a	n/a	n/a	n/a	n/a	n/a	n/a	n/a	n/a	n/a	n/a	n/a	n/a	n/a	n/a	n/a	n/a	n/a	n/a	n/a
Yb	1379	1354	1161	1826	1491	1385	683	745	888	1050	584	745	726	609	950	876	563	894	910	1012	901	852

Ti-in-zircon thermometry for this sample was calculated using the calibration of Watson et al., [52]. While this sample contains a Ti-phase (rutile), it does not contain quartz, and therefore, the activity of silica (a_{Si}) is not precisely known. Thus, the temperatures reported here are minima [53]. The range of calculated temperatures and Ti contents are listed in Table 7. The mean temperatures for concordant zircon core domains is 708 ± 26 °C (2σ), while the mean for concordant rim domain zircon is 668 ± 26 °C (2σ).

Table 7. Ti-in zircon thermometry.

Grain	Long Axis (μm)	Short Axis (μm)	Textural Setting	Spot	Domain	Ti (ppm)	Ti-in-Zrn Thermometry	
							2σ	T (C°)
z17	110	70	Pl/Bt g.b	1	Core	4.8	1.3	680
z8	40	30	Pl g.b	2	Core	5.5	1.6	691
z21	60	45	Pl	3	Core	13.2	3.8	766
s* z17	40	25	n/a	1	Core	8.9	2.6	731
z8	40	30	Pl	1	Core	8.8	2.5	730
z17	110	70	Pl/Bt g.b	4	Core	4.3	1.1	672
s z21	100	55	n/a	1	Core	7.3	1.4	714
z88	60	50	Pl	1	Core	4.3	1.3	672
s z26	120	100	n/a	1	Core	4.6	1.3	677
z21	60	45	Pl g.b	2	Core	7.4	1.3	715
s z16	100	50	n/a	1	Core	6.2	2.2	701
z20	70	45	Pl	3	Core	8.1	2.5	723
s z18	100	60	n/a	1	Core	6.9	1.2	709
z9	45	40	Pl	2	Core	7.7	1.8	719
z53	45	45	Pl	2	Core	7.1	1.6	712
s z17	40	25	n/a	2	Core	8.3	2.6	725
z17	110	70	Pl/Bt g.b	2	Core	15	3.8	778
z16	40	30	Pl/Mnz/Rt g.b.	2	Core	1600	1300	n/a
z21	60	45	Pl g.b	1	Core	17	2.2	790
z54	80	70	Pl g.b	2	Core	28.3	3.1	841
s z1	100	50	n/a	1b	Core	8	2.5	722
z59	40	30	Bt w/Mnz	4	Core	18.2	2	796
z34	200	80	Pl/Bt g.b	5	Core	1840	490	n/a
z54	80	70	Pl g.b	1	Core	14.1	1.9	772
z54	80	70	Pl g.b	3	Core	18.1	2.4	796
z89L	50	30	Pl	1	Core	34	7.7	861
z2	70	60	Pl/Bt g.b	4	Core	24.6	5.6	827
z85	150	50	Pl	6	Core	19.3	4.4	802
z9	45	40	Pl	1	Core	10.4	2.3	744
z85	150	50	Pl	2	Core	8.3	1.7	725
z59	40	30	Bt w/Mnz	3	Core	74	35	954
z20	70	45	Pl	1	Core	31.3	5.6	852
s z24	60	60	n/a	1	Core	7.8	2.3	720
z85	150	50	Pl	5	Core	17.2	3.7	791
z59	40	30	Bt w/Mnz	1	Core	20.4	2.9	808
z85	150	50	Pl	4	Core	19.1	3	801
z31	60	60	Pl g.b	3	Core	19	2.3	801
s z1	100	50	n/a	2	Rim	26.7	6	835
z19	70	45	Pl	1	Core	5.7	1.6	694
z16	40	30	Pl/Mnz/Rt g.b.	1	Core	69	23	945
z53	45	45	Pl	1	Core	57.1	7.7	921
s z1	100	50	n/a	3	Core	3.3	1.4	652
z19	70	45	Pl	2	Core	15.9	2.9	783
z34	200	80	Pl/Bt g.b	2	Core	17.2	2.6	791
z2	70	60	Pl/Bt g.b	1	Core	49.5	6.8	904
s z26	120	100	n/a	2	Core	8.3	1.9	725
z34	200	80	Pl/Bt g.b	4	Core	157	79	1059
z34	200	80	Pl/Bt g.b	3	Core	65	13	937
z20	70	45	Pl	2	Core	95	12	987
z2	70	60	Pl/Bt g.b	3	Core	87	25	975
z34	200	80	Pl/Bt g.b	1	Core	83	15	969
z2	70	60	Pl/Bt g.b	2	Core	62.3	4.1	932
z85	150	50	Pl	3	Rim	3.8	1.6	663
z31	60	60	Pl g.b	4	Rim	6.2	2.7	701
z66	30	20	Pl/Rt g.b	1	Rim/whole	3.5	1.5	656
z76	60	20	Bt	1	Rim	2.5	1.5	632
z31	60	60	Pl g.b	1	Rim	5.9	1.3	697
s z1	100	50	n/a	1a	Rim	3.7	1.4	661

Table 7. *Cont.*

Grain	Long Axis (μm)	Short Axis (μm)	Textural Setting	Spot	Domain	Ti (ppm)	Ti-in-Zrn Thermometry	
							2σ	T (C°)
z31	60	60	Pl g.b	5	Rim	13.7	1.9	769
z59	40	30	Bt w/Mnz	2	Mix	350	180	1193
z31	60	60	Pl g.b	2	Mix	13.7	1.9	769
z85	150	50	Pl	7	Mix	61	12	929
z85	150	50	Pl	1	Mix	61	12	929
z7	40	30	Pl	1	Mix	61000	36000	n/a
z85	150	50	Pl	8	Mix	162	48	1064
z17	110	70	Pl/Bt g.b	3	Mix	390	240	1213
z73	40	25	Pl/Bt g.b	1	Mix	370	300	1203
z89U	50	40	Pl/Bt g.b	1	Mix	61	23	929
s z26	120	100	n/a	3	Mix	32.2	7.7	855

* s before grain indicates zircon separate analyses; g.b. grain boundary.

6. Discussion

6.1. Origin of the Albitite

We consider both magmatic and metasomatic potential origins for the albitite within Bear Basin, and evaluate field relationships, geochemistry, and textural and mineralogical data for each mechanism. While igneous albitite has been reported in some localities (e.g., [54]), these occurrences are rare compared to metasomatic albitites [17]. The meter-scale tabular or lenticular geometry of the Bear Basin albitite is quite similar to several other tabular white rock bodies that crop out within the biotite ± garnet gneiss in the region (Figure 2E). However, whereas the latter, which are leucogranite dikes, have sharp contacts with their host, the one exposed contact of the albitite is an undulose gradational contact that transitions to the porphyroclastic granodiorite over ~5 cm (Figure 2A).

Bulk rock geochemical analysis indicates that the albitite composition is quite different than the granite sheets, which are peraluminous leucogranites (Table 2). The albitite has lower SiO_2 than the leucogranite sheets (~62 wt % vs >71 wt %, Table 2), and is much more enriched in LREE (Figure 5). Typical granitoid rocks altered by albitization have elevated Na_2O content, and low CaO and K_2O contents [17], which we observe in the albitite bulk rock geochemistry. By contrast, partial melting of the surrounding orthogneiss (e.g., tonalitic gneiss) or metasedimentary units would result in partial melts with either tonalitic compositions [55] or peraluminous high silica granites [56] similar to the composition of the leucogranite sheets.

Within the albitite, the occurrence of unzoned albitic feldspar, quartz free assemblages, and anthophyllite are uncharacteristic features of magmatic rocks. Albite is a common metasomatic product of Na-rich fluids [17,57,58] moving through the crust and altering granitoids. During this alteration process, quartz can be consumed to facilitate the transformation of Al-rich anorthite feldspar into Si-rich albite (e.g., [17,59]). If this albitization occurred at high temperature conditions, it explains the pristine textural appearance of the albite within the albitite (Figure 4B,C), which facilitated annealing of any porosity that developed during albitization of the feldspar. Anthophyllite is unknown to occur within magmatic rocks, and typically forms during metamorphism or metasomatism [60].

Accessory mineral textures within the albitite and the surrounding rocks also aid in constraining the albitite origin. Zircon glomerocrysts only occur within the albitite, suggesting that perhaps this texture is related to the same processes that produced this rock. The glomerocrysts consist of several small zircon dark CL cores surrounded and welded together by bright zircon rims (e.g., Figure 9C,D,G; Figure A2B). Importantly, EBSD data indicate each small zircon grain welded together has a different orientation (Figure 9C). We envision several potential models for glomerocryst formation. The first possibility is that these textures are inherited from igneous processes, either as a single originally igneous zircon that fractured during syn-magmatic deformation, or as separate zircon grains that amalgamated in a complex fluid dynamic environment at the edge of a cooling pluton. This process could have been similar to velocity-gradient or gravitational sorting mechanisms that have been

proposed to explain mafic enclave concentrations at the margins of plutons (e.g., [61]). Regardless of the precise mechanism, the salient point for this scenario is that the glomerocrystic texture is inherited from a syn-zircon core crystallization (e.g., 3.2 Ga) magmatic feature. These core domain fragments or grains were subsequently welded together by bright CL rim material during a later zircon growth event. Inclusion of these glomerocrysts in twinned but otherwise undeformed feldspar (although albitized; e.g., Figure 9G) support this interpretation, and it is our preferred one. A second possibility is that the glomerocrystic texture is a product of deformation of a single zircon dark CL core grain during fluid flow and alteration. In this scenario, the glomerocrysts formed during dissolution and reprecipitation of new bright CL zircon rim material along fractures or cracks (e.g., Figure 9D,G; Figure A2). This may indicate an intermediate step in glomerocryst formation during dissolution–reprecipitation, however, it does not fully explain the variable zircon subgrain orientations. If the albitite has an igneous origin, a third possibility is that the glomerocrysts are sourced from small scale cumulates or locally entrained residue that developed during partial melting of the presumed protolith.

Collectively, we interpret the field relationships, bulk rock composition, and mineral assemblages (e.g., Ab + OAm) and textures, as supporting a metasomatic origin for the albitite. A remaining question is what was the protolith (i.e. what was metasomatized and transformed). Given the location of the albitite along the boundary between the biotite ± garnet gneiss and the granodiorite, which may well have acted as an efficient pathway for fluid infiltration and alteration, it is plausible that one of these lithologies is the protolith. By using zircon geochronology, morphology, and texture, a direct link between the metasomatic product and protolith can be made. We interpret the zircon cores to be inherited from the original protolith and partially preserved during metamorphism and metasomatism. Therefore, core ages and morphologies should fingerprint the rock transformed into the albitite during metasomatism. Zircon cores exhibit oscillatory zoning characteristic of igneous zircon (e.g., [62]) and grew at 3175 ± 23 Ma. This age is identical within error to the crystallization age of the porphyroclastic granodiorite of 3177 ± 36 Ma, and considerably older than the 2868 ± 34 Ma age of zircon in the biotite ± garnet gneiss [34]. This timing of core domain zircon and porphyroclastic granodiorite crystallization also overlaps with crystallization of the Hbl monzodiorite and the tonalitic gneiss from the same area (Figure 1C, [34]). However, the zircon textures preclude either of these lithologies as possible protoliths, with only the porphyroclastic granodiorite exhibiting consistent oscillatory zoned zircon textures (Figure 10; Figure A3).

6.2. Chemical Transformation to Albitite

Because metasomatic alteration of the granodiorite is our preferred model for albitite formation, the chemical transformation from the granodiorite to the albitite is plotted as an isocon diagram in Figure 12A. Such diagrams are useful when assessing metasomatic gain or loss of chemical components in altered vs unaltered rock [63,64]. If we assume no volume change, elements that plot above the dashed black line (1:1 line) indicate gain from granodiorite to albitite, while elements plotting below this line indicate loss. It is entirely possible that this system experienced a net volume change. However, there is not an obvious set of immobile elements that plot along a single array that would define an isocon slope. Thus, we feel confident in the trends of elements that experienced the greatest gains or losses. Given this, the isocon analysis shows a loss in CaO, Fe_2O_3, K_2O, Ba, Sr, Rb, Co, and MnO, and a gain of Y, MgO, Dy, Na_2O, Er, and Yb (Figure 12A,B).

This transformation is characteristic of the metasomatic effects recognized in other albitized granitoids. For example, Kaur et al., [65] showed major gains in Na and losses of K, Rb, Fe, and Ba between albitites and unaltered protoliths, and similar observations have been made in other albitite studies [59,66]. Thus, the albitite in Bear Basin is interpreted to be a metasomatized, marginal component of the porphyroclastic granodiorite pluton, and mineral textures with high angle grain boundaries (e.g., Figure 4B) indicate that this process likely occurred at relatively high temperatures. To understand when this fluid flow and metasomatism occurred, we turn to the monazite and zircon trace element geochemistry and geochronology data.

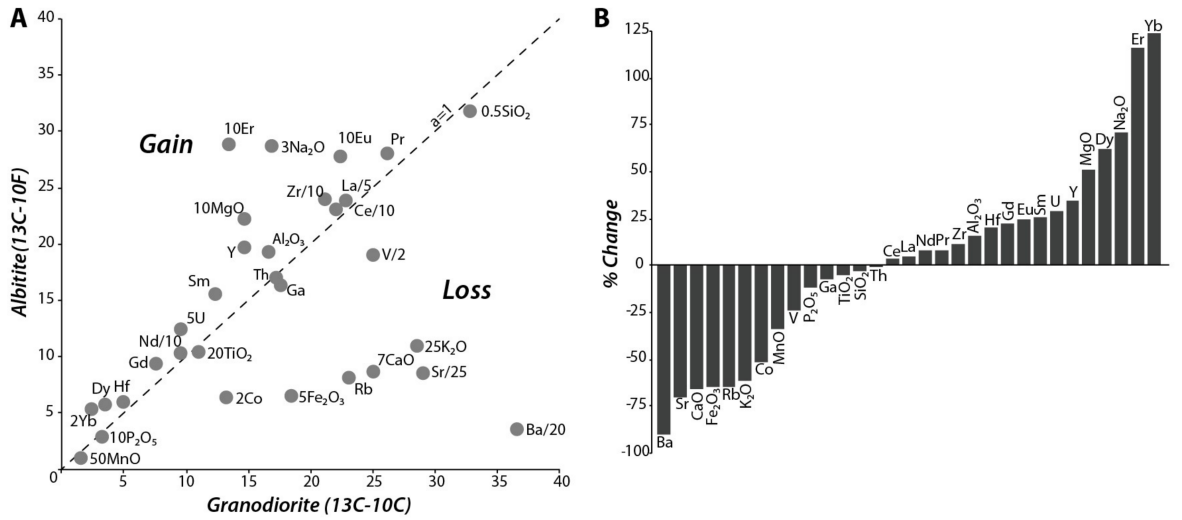

Figure 12. (**A**) Isocon diagram showing relative loss and gain of chemical constituents between the protolith granodiorite (sample 13c-10c) and the albitite (sample 13c-10f) assuming no volume change. Elements gained during metasomatism generally plot above the 1:1 dashed line (a = 1), and elements lost during metasomatism generally plot below this line. Scaling factors have been added to some elements; (**B**) Calculated percent change for elements between the protolith and metasomatized product assuming no volume change.

6.3. Direct Dating Constraints on Albitization and Fluid Flow

The foliation in the albitite, defined by synmetasomatic anthophyllite and biotite (Figure 2C), is parallel to S_2, which formed during the main phase of Paleoproterozoic deformation at ca. 1740–1720 Ma (Figure 13, [20]). However, it is possible that the actual metasomatic process took place before this thermotectonism and the high temperature textures represent annealing during subsequent metamorphism. Therefore, we use accessory mineral geochronology linked to geochemistry and textural appearance to constrain the timing of fluid flow within this rock and, by extension, this region. Zircon cores have a weighted mean age of 3175 ± 23 Ma, and zircon rims have an age of 1750 ± 39 Ma. Monazite cores have a weighted mean age of 1750 ± 23 Ma, and rims a weighted mean age of 1734 ± 10 Ma. Below, we discuss how these two accessory mineral phases can dissolve and reprecipitate during fluid flow, with newly reprecipitated rim domains carrying a geochemical fingerprint of albitization.

Both monazite and zircon are known to readily grow during fluid flow events [13,14,67,68]. In both phases, coupled dissolution of the existing phase and reprecipitation of new zircon or monazite is facilitated by the external fluid, and Pb is generally expelled from the newly reprecipitated domains [69–71]. Thus, the geochronological system is reset, and can be used to date the timing of fluid flow.

Experimental and natural studies [69–73] show that new monazite and zircon can grow at high P-T conditions in the presence of sodic fluids. This process is facilitated by the exchange of elements from the fluid, with the existing monazite or zircon by the formation of micrometer scale porosity in the dissolution–reprecipitation reaction front [67,74]. However, these pores may or may not be preserved after formation [75]. Morphologically, the newly precipitated phase generally crosscuts any zoning present in the original grain along sharp dissolution–precipitation fronts, and can occur as patchy growths and psuedomorphs [74,76–79]; similar textures to those observed here in the multidomainal monazite (e.g., Figure 6A–C) and zircon (e.g., Figure 9A–D,G; Figure A2).

Geochemical signatures of fluid related dissolution–reprecipitation from experimentally grown and naturally investigated monazite and zircon provide useful constraints for identifying new phase growth during sodic fluid flow. Experimentally reprecipitated monazite is typically higher in Th

and lower in Y and HREE than the original monazite. Th is less compatible with the Na-rich fluid than monazite, and returns to the mineral during reprecipitation, whereas the Y and HREE are more compatible with the fluid [70]. Reprecipitated zircon growing during Na-Ca rich fluid flow typically has lower Th, REE and other trace elements than the original zircon [67,69,80].

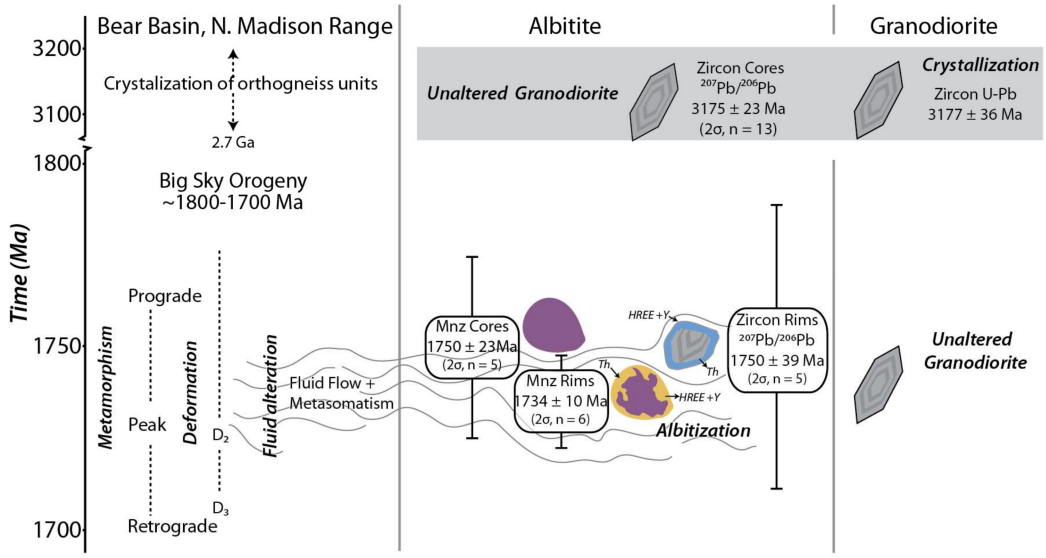

Figure 13. Schematic time-process diagram of the evolution of the Bear Basin region, the albitite, and the porphyroclastic granodiorite from Mesoarchean crystallization of major orthogneiss units to the end of the Late Paleoproterozoic Big Sky Orogeny. See text for discussion. Granodiorite U-Pb zircon data from [34]. Timing of processes from the Big Sky orogeny from [20].

The above chemical patterns are observed in both the monazite and zircon investigated here (Figure 8). Monazite core domains have several zones high in Th, but the majority of the cores have dramatically lower Th concentrations (<9000 ppm) compared to monazite rim domains (>~16,000 ppm). Observed Y content and HREE patterns also match experimental observations; monazite rims generally have lower Y and HREE than cores (Table 3; Figure 6A–C; Figure 8A). Zircon rims have very low Th content (~0–7 ppm) (Table 5; Figure 8D) and lower LREE and MREE and higher HREE than zircon core domains (Table 6; Figure 8B). This can be explained both by coupled dissolution–reprecipitation of zircon with a fluid and with concurrent growth with monazite rims. LREE and MREE released from the pre-existing zircon would have been more compatible with the fluid, and would not have been incorporated into the new zircon rims. Similarly, as monazite rims grew within this same fluid, Y and HREE within the original monazite core domains would not have reprecipitated, and instead, would have moved into the fluid (Figure 13). As zircon rim material grew in the presence of this fluid, it would have preferentially taken up the HREE released by the dissolving monazite. Together, monazite and zircon rim geochemistry and textures indicate that the rim domains grew metasomatically during albitization and Na-fluid flow at 1750–1735 Ma.

6.4. Tectonic Significance of Metasomatism and Regional Fluid Flow

Lithological and field evidence indicate pervasive fluid flow in the Bear Basin region during the late Paleoproterozoic Big Sky orogeny including penetrative regional D_2 fabric defined by synkinematic hydrous phases (Figure 2C, [20]) and garbenschiefer textures directly linked to monazite and zircon geochronology. Zircon and monazite from a deformed mafic dike and the Bear Basin pelitic schist, respectively constrain the deformation and associated prograde to peak metamorphism, (0.9 GPa and ~700 °C), to have occurred in the interval of 1750–1720 Ma [20] (Figure 7B; Figure 13). Our new results are consistent with this pattern. Monazite cores from the albitite grew early during this same

interval, followed by growth of rims of both monazite and zircon in conjunction with fluid infiltration (Figure 13). The minimum temperatures from Ti concentrations in zircon rims (668 ± 26 °C; 2σ) are consistent with the peak temperature suggested by Condit et al. [20].

The source of the fluids within this region remains unclear. The occurrence of albitization constrains the composition of at least some of the fluids as Na-rich. Within the Big Sky orogeny, a pattern of southeastward propagation of hinterland thermotectonism towards the foreland is recorded in zircon, monazite, and garnet geochronology across ~100 km and over an ~80–40 myr timespan from 1.80–1.78 Ga in the Highland and Ruby Ranges (Figure 1) to 1.75–1.72 Ga in Northern Madison Range [20]. This pattern offers a tectonic framework to begin speculating on the sources of these fluids. As the Big Sky orogen's metamorphic core grew, thrusting and burial of sedimentary rocks may have resulted in prograde metamorphism and subsequent dehydration below the area of Bear Basin, and these fluid may have infiltrated and facilitated metasomatism and metamorphism. At a more local scale, the metapelitic schist found within Bear Basin itself would be undergoing prograde metamorphism and dewatering during this period, which could cause originally low salinity fluids to become locally enriched [81], resulting in nearby local albitization. The protolith and depositional nature of this heterogeneous schist remains unconstrained. However, observations of conglomeratic layers along its contacts (Figure 1C, [20]) suggest it could have a terrestrial origin. It is possible that thin evaporite layers may have released sodium to increase salinity in the dewatering metamorphic fluids. In the nearby Tobacco Root Mountains (Figure 1A), another package of metavolcaniclastic and metasedimentary rocks, the Spuhler Peak metamorphic suite, preserves similar fluid-related and metasomatic features to those observed in Bear Basin [82]. These rocks appear to record another locus of metasomatism and alteration within the Big Sky orogeny. Regardless of the fluid source, the end result is a region of pervasive metamorphism, areas of metasomatism, and penetrative fabric development during the interval of 1750–1720 Ma in the northern Gallatin Peak terrane.

7. Conclusions

Albitization along the margin of an Archean granodioritic orthogneiss resulted in complete transformation of plagioclase and K-feldspar to almost pure albite. During metasomatism, orthoamphibole and biotite grew synkinematically in alignment with the regional D_2 foliation fabric. Na-rich fluids metasomatized this rock, resulting in an increase in Na and a marked decrease in Ca, K, Ba, Fe, and Sr. Monazite and zircon geochronology, morphology, textures and trace element geochemistry link the timing of this metasomatism to prograde peak metamorphism and deformation of the Big Sky orogeny, from 1750–1720 Ma. It is through the coupling of these textural, geochronological, and geochemical techniques that a robust interpretation of the timing of amphibolite facies metasomatism is established.

Author Contributions: C.B.C. and K.H.M. designed the experiments. C.B.C., K.H.M., K.C.C. and A.M. collected and interpreted the data. C.B.C. wrote the paper with significant contributions from K.H.M., A.M. and K.C.C. C.B.C. and K.C.C. prepared the figures.

Acknowledgments: Funding for this work was provided by NSF grant (EAR1252295) to Mahan, USGS EDMAP grant to Mahan and Condit, and the Spetzler Research Award from the University of Colorado, Department of Geological Sciences to Condit. N. Kelly, J. Allaz, and R. Flowers are thanked for their comments on an earlier draft. Invaluable field assistance was provided by K. Kravitz, K. Toenenboehn, and D. Rattanasith. Detailed reviews from Samuel Angiboust and three anonymous reviewers improved the quality of this work and are thanked.

Conflicts of Interest: There are no known conflicts of interest

Appendix

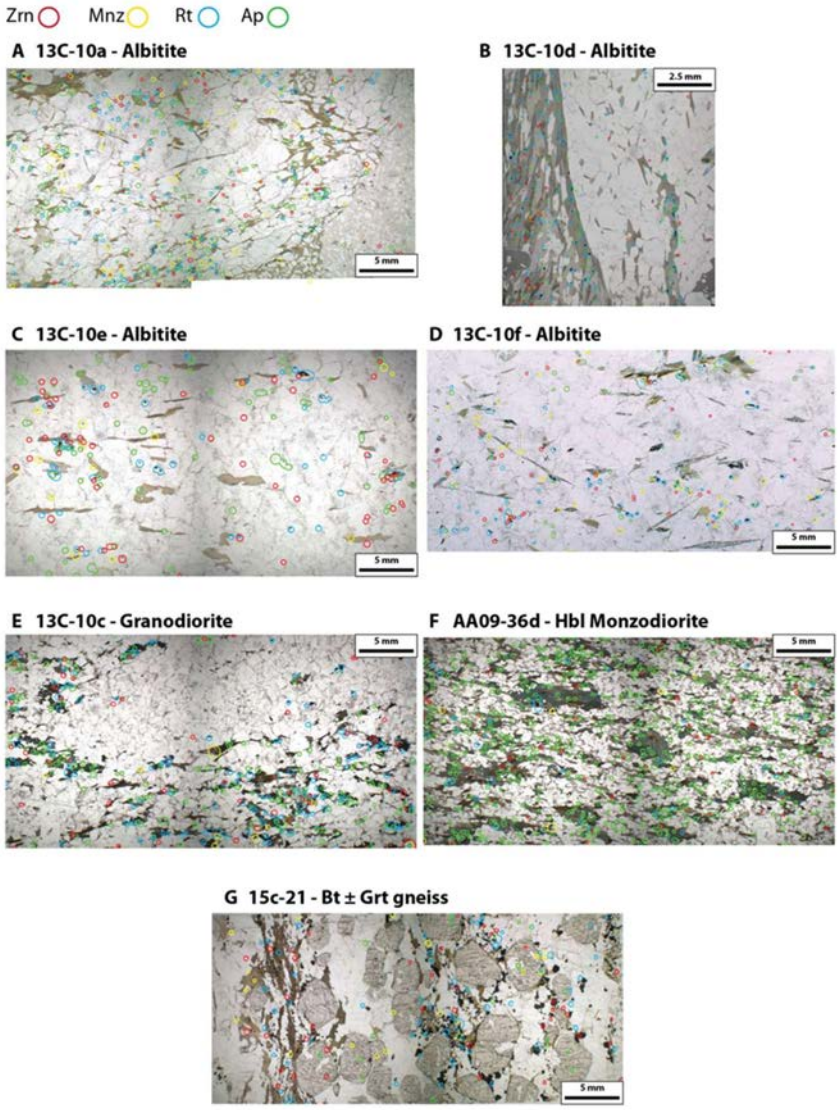

Figure A1. Full thin section photomicrographs showing locations of accessory minerals (zircon, monazite, rutile, and apatite) detected using full thin section WDS search maps (Al, Zr, Ce, Ti, and P) later registered to the photomicrograph. (**A**) Albitite sample 13c-10a; (**B**) Albitite sample 13c-10d; (**C**) Albitite sample 13C-10e; (**D**) Albitite sample 13c-10f; (**E**) Porphyroclastic granodiorite sample 13c-10c. (**F**) Hbl Monzodiorite sample AA09-36d; (**G**) biotite ± garnet gneiss sample 15c-21.

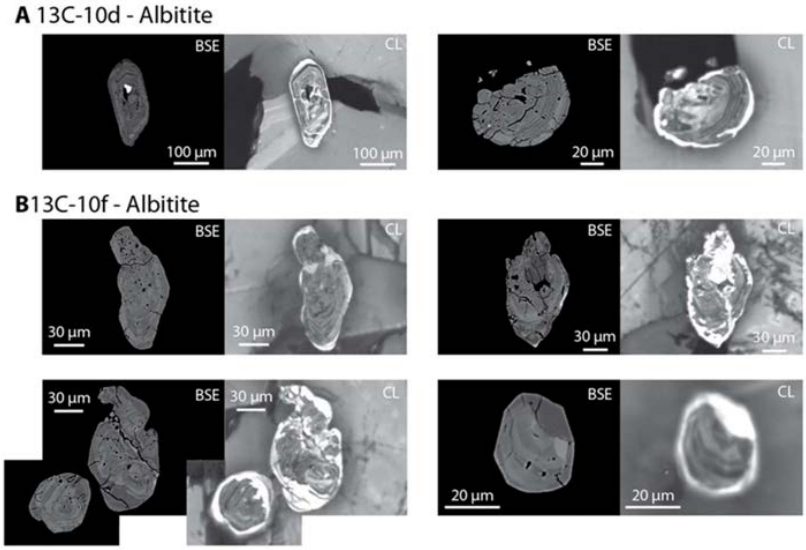

Figure A2. BSE and CL images of zircon from albitite samples (**A**) 13c-10d and (**B**) 13c-10f. All zircon grains show dark CL cores with concentric zoning and bright CL rims that truncate core zoning.

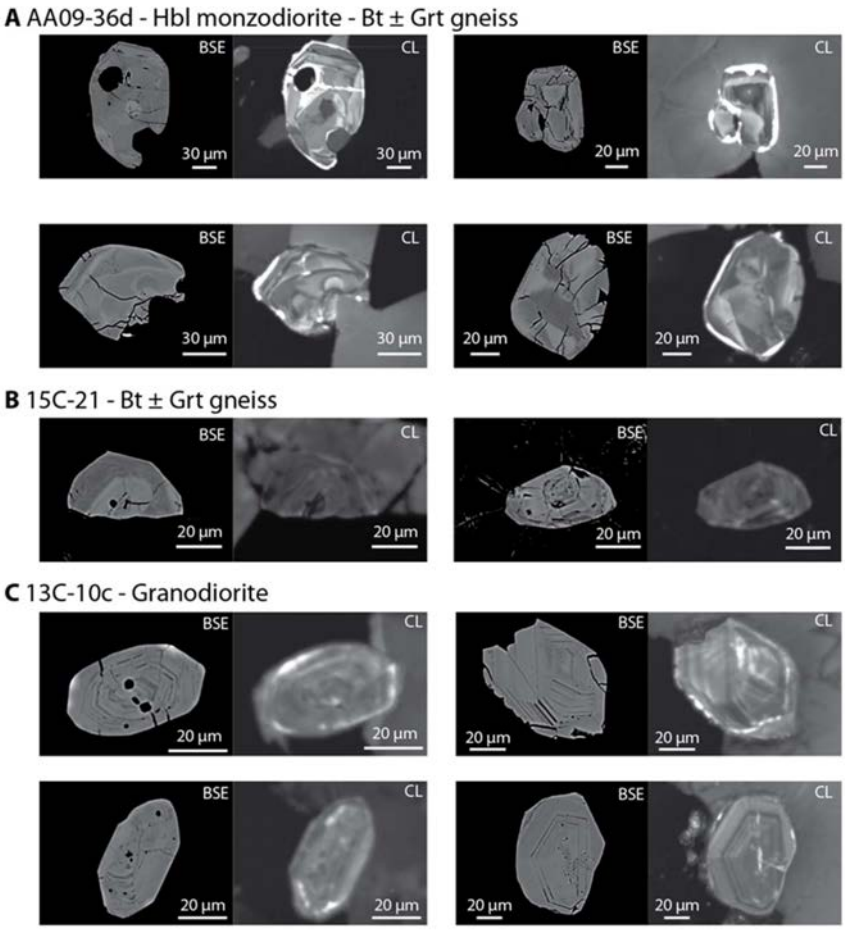

Figure A3. BSE and CL image of zircon from non-albitite samples. (**A**) Hbl monzodiorite sample AA09-36 zircon show complicated internal sector zoning with bright CL rims; (**B**) Biotite ± garnet sample 15c-21 zircon show complicated internal zoning and no bright CL rims; (**C**) Porphyroclastic granodiorite sample 13c-10c show well developed concentric zoning, rational crystal faces, and little to no bright CL rim materials.

References

1. Jamtveit, B.; Austrheim, H.; Putnis, A. Disequilibrium metamorphism of stressed lithosphere. *Earth Sci. Rev.* **2016**, *154*, 1–13. [CrossRef]
2. Goncalves, P.; Oliot, E.; Marquer, D.; Connolly, J.A.D. Role of chemical processes on shear zone formation: An example from the Grimsel metagranodiorite (Aar massif, Central Alps). *J. Metamorph. Geol.* **2012**, *30*, 703–722. [CrossRef]
3. Condit, C.B.; Mahan, K.H. Fracturing, fluid flow and shear zone development: Relationships between chemical and mechanical processes in Proterozoic mafic dykes from southwestern Montana, USA. *J. Metamorph. Geol.* **2018**, *36*, 195–223. [CrossRef]
4. Penniston-Dorland, S.C.; Ferry, J.M. Element mobility and scale of mass transport in the formation of quartz veins during regional metamorphism of the Waits River Formation, east-central Vermont. *Am. Mineral.* **2008**, *93*, 7–21. [CrossRef]
5. Ague, J.J. Mass-transfer during Barrovian metamorphism of pelites, south-central Connecticut I: Evidence for changes in composition and volume. *Am. J. Sci.* **1994**, *294*, 989–1057. [CrossRef]
6. Jones, C.H.; Mahan, K.H.; Butcher, L.A.; Levandowski, W.B.; Farmer, G.L. Continental uplift through crustal hydration. *Geology* **2015**, *43*, 355–358. [CrossRef]
7. Fischer, K.M. Waning buoyancy in the crustal roots of old mountains. *Nature* **2002**, *417*, 933–936. [CrossRef] [PubMed]
8. Humphreys, E.; Hessler, E.; Dueker, K.; Farmer, G.L.; Erslev, E.; Atwater, T. How Laramide-Age Hydration of North American Lithosphere by the Farallon Slab Controlled Subsequent Activity in the Western United States. *Int. Geol. Rev.* **2003**, *45*, 575–595. [CrossRef]
9. Breeding, C.M.; Ague, J.J. Slab-derived fluids and quartz-vein formation in an accretionary prism, Otago Schist, New Zealand. *Geology* **2002**, *30*, 499–502. [CrossRef]
10. Audet, P.; Bürgmann, R. Possible control of subduction zone slow-earthquake periodicity by silica enrichment. *Nature* **2014**, *510*, 389–392. [CrossRef] [PubMed]
11. Goncalves, P.; Marquer, D.; Oliot, E.; Durand, C. Thermodynamic Modeling and Thermobarometry of Metasomatized Rocks. In *Metasomatism and Chemical Transformation of Rock*; Harlov, D.E., Austrheim, H., Eds.; Springer: Berlin, Germany, 2013; pp. 53–92. ISBN 978-3-642-28393-2.
12. Yardley, B. The Chemical Composition of Metasomatic Fluids in the Crust. In *Metasomatism and the Chemical Transformation of Rock*; Harlov, D.E., Austrheim, H., Eds.; Springer: Berlin, Germany, 2013; pp. 17–51.
13. Villa, I.M.; Williams, M.L. Geochronology of Metasomatic Events. In *Metasomatism and the Chemical Transformation of Rock SE—8*; Springer: Berlin, Germany, 2013; pp. 171–202. ISBN 978-3-642-28393-2.
14. Mahan, K.H.; Goncalves, P.; Williams, M.L.; Jercinovic, M.J. Dating metamorphic reactions and fluid flow: Application to exhumation of high-P granulites in a crustal-scale shear zone, western Canadian Shield. *J. Metamorph. Geol.* **2006**, *24*, 193–217. [CrossRef]
15. Butcher, L.; Mahan, K.H.; Allaz, J.M. Late Cretaceous crustal hydration in the Colorado Plateau, USA, from xenolith petrology and monazite geochronology. *Lithosphere* **2017**, *9*, 561–578. [CrossRef]
16. Rubatto, D.; Angiboust, S. Oxygen isotope record of oceanic and high pressure metasomatism: A P-T-time-fluid path for the Monviso eclogite (Italy). *Cont. Min. Pet.* **2015**, *170*. [CrossRef]
17. Engvik, A.K.; Putnis, A.; Fitz Gerald, J.D.; Austrheim, H. Albitization of granitic rocks: The mechanism of replacement of oligoclase by albite. *Can. Mineral.* **2008**, *46*, 1401–1415. [CrossRef]
18. Petersson, J.; Stephens, M.B.; Mattsson, H.; Möller, C. Albitization and quartz dissolution in Paleoproterozoic metagranite, central Sweden-Implications for the disposal of spent nuclear fuel in a deep geological repository. *Lithos* **2012**, *148*, 10–26. [CrossRef]
19. Touret, J.; Nijland, T. Prograde, Peak and Retrograde Metamorphic Fluids and Associated Metasomatism in Upper Amphibolite to Granulite Facies Transition Zones. In *Metasomatism and the Chemical Transformation of Rock*; Harlov, D.E., Austrheim, H., Eds.; Springer: Berlin, Germany, 2013; pp. 415–469, ISBN 978-3-642-28393-2.
20. Condit, C.B.; Mahan, K.H.; Ault, A.K.; Flowers, R.M. Foreland-directed propagation of high-grade tectonism in the deep roots of a Paleoproterozoic collisional orogen, SW Montana, USA. *Lithosphere* **2015**, *7*, 625–645. [CrossRef]

21. Mueller, P.A.; Burger, H.R.; Wooden, J.L.; Heatherington, A.L.; Mogk, D.W.; D'Arcy, K. Age and evolution of the Precambrian Crust of the Tobacco Root Mountains, Montana. *Geol. Soc. Am. Spec. Pap.* **2004**, *377*, 181–202.
22. Harms, T.A.; Brady, J.B.; Burger, H.R.; Cheney, J.T. Advances in the geology of the Tobacco Root Mountains, Montana and their implications for the history of the northern Wyoming province. *Geol. Soc. Am. Spec. Pap.* **2004**, *377*, 227–243.
23. Mueller, P.A.; Burger, H.R.; Wooden, J.L.; Brady, J.B.; Cheney, J.T.; Harms, T.A.; Heatherington, A.L.; Mogk, D.W. Paleoproterozoic Metamorphism in the Northern Wyoming Province: Implications for the Assembly of Laurentia. *J. Geol.* **2005**, *113*, 169–179. [CrossRef]
24. Cheney, J.; Brady, J. Proterozoic metamorphism of the Tobacco Root Mountains, Montana. *Geol. Soc. Am. Spec. Pap.* **2004**, *377*, 105–129.
25. Krogh, T.E.; Kamo, S.L.; Hanley, T.B.; Hess, D.F.; Dahl, P.S.; Johnson, R.E. Geochronology and geochemistry of Precambrian gneisses, metabasites, and pegmatite from the Tobacco Root Mountains, northwestern Wyoming craton, Montana. *Can. J. Earth Sci.* **2011**, *48*, 161–185. [CrossRef]
26. Cheney, J.; Webb, A.; Coath, C.; McKeegan, K. In situ ion microprobe 207Pb/206Pb dating of monazite from Precambrian metamorphic suites, Tobacco Root Mountains, Montana. *Geol. Soc. Am. Spec. Pap.* **2004**, *377*, 151–179. [CrossRef]
27. Mueller, P.A.; Wooden, J.L.; Mogk, D.W.; Foster, D.A. Paleoproterozoic evolution of the Farmington zone: Implications for terrane accretion in southwestern Laurentia. *Lithosphere* **2011**, *3*, 401–408. [CrossRef]
28. Foster, D.A.; Mueller, P.A.; Mogk, D.W.; Wooden, J.L.; Vogl, J.J. Proterozoic evolution of the western margin of the Wyoming craton: Implications for the tectonic and magmatic evolution of the northern Rocky. *Can. J. Earth Sci.* **2006**, *43*, 1601–1619. [CrossRef]
29. Whitmeyer, S.; Karlstrom, K. Tectonic model for the Proterozoic growth of North America. *Geosphere* **2007**. [CrossRef]
30. Giletti, B. Isotopic ages from southwestern Montana. *J. Geophys. Res.* **1966**, *71*, 4029–4036. [CrossRef]
31. Giletti, B. Discordant isotopic ages and excess argon in biotites. *Earth Planet. Sci. Lett.* **1971**, *10*, 157–164. [CrossRef]
32. Hames, W.E.; Harms, T.A. Laser $^{40}Ar/^{39}Ar$ thermochronology of single crystals from Paleoproterozoic and Archean rocks of the norther Wyoming Province, Big Sky orogen, and Great Falls Tectonic Zone: Giletti's Line revisted. In Proceedings of the GSA's 125th Anniversary Annual Meeting & Exposition, Denver, CO, USA, 27–30 October 2013.
33. Salt, K.J. Archean Geology of the Spanish Peaks Area, Southwestern Montana, Montana State University. Master Thesis, Montana State University, Bozeman, MT, USA, March 1987.
34. Weyand, E.L. U-Pb Zircon geochronology of Archean Rocks from the Spanish Peaks area, Madison Range. Master's Thesis, Univeristy Of Florida, Gainesville, FL, USA, 1989.
35. Spencer, E.; Kozak, S. Precambrian evolution of the Spanish Peaks area, Montana. *Geol. Soc. Am. Bull.* **1975**, *86*, 785–792. [CrossRef]
36. Ault, A.K.; Flowers, R.M.; Mahan, K.H. Quartz shielding of sub-10µm zircons from radiation damage-enhanced Pb loss: An example from a metamorphosed mafic dike, northwestern Wyoming craton. *Earth Planet. Sci. Lett.* **2012**, *339–340*, 57–66. [CrossRef]
37. Whitney, D.L.; Evans, B.W. Abbreviations for names of rock-forming minerals. *Am. Mineral.* **2009**, *95*, 185–187. [CrossRef]
38. Mogk, D.W.; Mueller, P.A.; Wooden, J.L. The nature of Archean terrane boundaries: An example from the northern Wyoming Province. *Precambrian Res.* **1992**, *55*, 155–168. [CrossRef]
39. McDonough, W.F.; Sun, S.S. The composition of the Earth. *Chem. Geol.* **1995**, *120*, 223–253. [CrossRef]
40. Dumond, G.; Mclean, N.; Williams, M.; Jercinovic, M.; Bowring, S. High-resolution dating of granite petrogenesis and deformation in a lower crustal shear zone: Athabasca granulite terrane, western Canadian Shield. *Chem. Geol.* **2008**, *254*, 175–196. [CrossRef]
41. Williams, M.L.; Jercinovic, M.J.; Goncalves, P.; Mahan, K. Format and philosophy for collecting, compiling, and reporting microprobe monazite ages. *Chem. Geol.* **2006**, *225*, 1–15. [CrossRef]
42. Jercinovic, M.; Williams, M.; Lane, E. In-situ trace element analysis of monazite and other fine-grained accessory minerals by EPMA. *Chem. Geol.* **2008**, *254*, 197–215. [CrossRef]

43. Allaz, J.M.; Williams, M.L.; Jercinovic, M.J.; Donavan, J. A new technique for electron microprobe trace element analysis: The multipoint background method. In Proceedings of the EMAS Annual Meeting, Angers, France, 15–19 May 2011; pp. 319–320.
44. Davis, W.J. (Geological Survey of Canada). Personal communication, 2007.
45. Allaz, J.M. (ETH, Zurich, Switzerland). Personal communication, 2015.
46. Jackson, S.E.; Pearson, N.J.; Griffin, W.L.; Belousova, E.A. The application of laser ablation-in ductively coupled plasma-mass spectrometry to in situ U-Pb zircon geochronology. *Chem. Geol.* **2004**, *211*, 47–69. [CrossRef]
47. Jochum, K.P.; Weis, U.; Stoll, B.; Kuzmin, D.; Yang, Q.; Raczek, I.; Jacob, D.E.; Stracke, A.; Birbaum, K.; Frick, D.A.; et al. Determination of reference values for NIST SRM 610-617 glasses following ISO guidelines. *Geostand. Geoanal. Res.* **2011**, *35*, 397–429. [CrossRef]
48. Sláma, J.; Košler, J.; Condon, D.J.; Crowley, J.L.; Gerdes, A.; Hanchar, J.M.; Horstwood, M.S.A.; Morris, G.A.; Nasdala, L.; Norberg, N.; et al. Plešovice zircon—A new natural reference material for U–Pb and Hf isotopic microanalysis. *Chem. Geol.* **2008**, *249*, 1–35. [CrossRef]
49. Paton, C.; Woodhead, J.D.; Hellstrom, J.C.; Hergt, J.M.; Greig, A.; Maas, R. Improved laser ablation U–Pb zircon geochronology through robust downhole fractionation correction. *Geochem. Geophys. Geosyst.* **2010**, *11*. [CrossRef]
50. Paton, C.; Hellstrom, J.; Paul, B.; Woodhead, J.; Hergt, J. Iolite: Freeware for the visualisation and processing of mass spectrometric data. *J. Anal. At. Spectrom.* **2011**, *26*, 2508. [CrossRef]
51. Petrus, J.A.; Kamber, B.S. VizualAge: A Novel Approach to Laser Ablation ICP-MS U-Pb Geochronology Data Reduction. *Geostand. Geoanal. Res.* **2012**, *36*, 247–270. [CrossRef]
52. Watson, E.B.; Wark, D.A.; Thomas, J.B. Crystallization thermometers for zircon and rutile. *Contrib. Mineral. Petrol.* **2006**, *151*, 413–433. [CrossRef]
53. Fu, B.; Page, F.Z.; Cavosie, A.J.; Fournelle, J.; Kita, N.T.; Lackey, J.S.; Wilde, S.A.; Valley, J.W. Ti-in-zircon thermometry: Applications and limitations. *Contrib. Mineral. Petrol.* **2008**, *156*, 197–215. [CrossRef]
54. Pin, C.; Monchoux, P.; Paquette, J.L.; Azambre, B.; Wang, R.C.; Martin, R.F. Igneous albitite dikes in orogenic lherzolites, western Pyrénées, France: A possible source for corundum and alkali feldspar xenocrysts in basaltic terranes. II. Geochemical and petrogenetic considerations. *Can. Mineral.* **2006**, *44*, 843–856. [CrossRef]
55. Nédélec, A.; Minyem, D.; Barbey, P. High-P-high-T anatexis of Archaean tonalitic grey gneisses: The Eseka migmatites, Cameroon. *Precambr. Res.* **1993**, *62*, 191–205. [CrossRef]
56. Thompson, A.B. Dehydration melting of pelitic rocks and the generation of H2O-undersaturated granitic liquids. *Am. J. Sci.* **1982**, *282*, 1567–1595. [CrossRef]
57. Rubenach, M.J.; Lewthwaite, K.A. Metasomatic albitites and related biotite-rich schists from a low-pressure polymetamorphic terrane, Snake Creek Anticline, Mount Isa Inlier, North-Eastern Australia: Microstructures and P-T-d paths. *J. Metamorph. Geol.* **2002**, *20*, 191–202. [CrossRef]
58. Engvik, A.K.; Ihlen, P.M.; Austrheim, H. Characterisation of Na-metasomatism in the Sveconorwegian Bamble Sector of South Norway. *Geosci. Front.* **2014**, *5*, 659–672. [CrossRef]
59. Boulvais, P.; Ruffet, G.; Cornichet, J.; Mermet, M. Cretaceous albitization and dequartzification of Hercynian peraluminous granite in the Salvezines Massif (French Pyrenees). *Lithos* **2007**, *93*, 89–106. [CrossRef]
60. Deer, W.; Howie, R.; Zussman, J. *The Rock Forming Minerals*, 2nd ed.; Pearson Education Limited: London, UK, 1992.
61. Tobisch, O.T.; McNully, B.A.; Vernon, R.H. Microgranitoid enclave swarms in granitic pluton, central Sierra Nevada, California. *Lithos* **1997**, *40*, 321–339. [CrossRef]
62. Corfu, F.; Hanchar, J.M.; Hoskin, P.W.; Kinny, P. Atlas of Zircon Textures. *Rev. Mineral. Geochem.* **2003**, *53*, 469–500. [CrossRef]
63. Grant, J.A. The isocon diagram; a simple solution to Gresens' equation for metasomatic alteration. *Econ. Geol.* **1986**, *81*, 1976–1982. [CrossRef]
64. Grant, M.L.; Wilde, S.A.; Wu, F.; Yang, J. The application of zircon cathodoluminescence imaging, Th–U–Pb chemistry and U–Pb ages in interpreting discrete magmatic and high-grade metamorphic events in the North China Craton at the Archean/Proterozoic boundary. *Chem. Geol.* **2009**, *261*, 155–171. [CrossRef]
65. Kaur, P.; Chaudhri, N.; Hofmann, A.W. New evidence for two sharp replacement fronts during albitization of granitoids from northern Aravalli orogen, northwest India. *Int. Geol. Rev.* **2015**, *57*, 1660–1685. [CrossRef]

66. Jaguin, J.; Boulvais, P.; Poujol, M.; Bosse, V.; Paquette, J.L.; Vilbert, D. Albitization in the Antimony Line, Murchison Greenstone Belt (Kaapvaal Craton): A geochemical and geochronological investigation. *Lithos* **2013**, *168–169*, 124–143. [CrossRef]
67. Geisler, T.; Schaltegger, U.; Tomaschek, F. Re-equilibration of zircon in aqueous fluids and melts. *Elements* **2007**, *3*, 43–50. [CrossRef]
68. Petrík, I.; Konečný, P. Metasomatic replacement of inherited metamorphic monazite in a biotite-garnet granite from the Nízke Tatry Mountains, Western Carpathians, Slovakia: Chemical dating and evidence for disequilibrium melting. *Am. Mineral.* **2009**, *94*, 957–974. [CrossRef]
69. Harlov, D.E.; Dunkley, D.J. Experimental high-grade alteration of zircon using alkali- and Ca-bearing solutions. *Am. Mineral.* **2011**, *96*, 716–731. [CrossRef]
70. Harlov, D.E.; Hetherington, C.J. Partial high-grade alteration of monazite using alkali-bearing fluids: Experiment and nature. *Am. Mineral.* **2010**, *95*, 1105–1108. [CrossRef]
71. Williams, M.L.; Jercinovic, M.J.; Harlov, D.E.; Budzyń, B.; Hetherington, C.J. Resetting monazite ages during fluid-related alteration. *Chem. Geol.* **2011**, *283*, 218–225. [CrossRef]
72. Hetherington, C.J.; Harlov, D.E.; Budzyń, B. Experimental metasomatism of monazite and xenotime: Mineral stability, REE mobility and fluid composition. *Mineral. Petrol.* **2010**, *99*, 165–184. [CrossRef]
73. Hurai, V.; Paquette, J.L.; Lexa, O.; Konečný, P.; Dianiška, I. U-Pb-Th geochronology of monazite and zircon in albitite metasomatites of the Rožňava-Nadabula ore field (Western Carpathians, Slovakia): Implications for the origin of hydrothermal polymetallic siderite veins. *Mineral. Petrol.* **2015**, *109*, 519–530. [CrossRef]
74. Putnis, A. Mineral Replacement Reactions. *Rev. Mineral. Geochem.* **2009**, *70*, 87–124. [CrossRef]
75. Putnis, A. Mineral replacement reactions: From macroscopic observations to microscopic mechanisms. *Mineral. Mag.* **2002**, *66*, 689–708. [CrossRef]
76. Tomaschek, F. Zircons from Syros, Cyclades, Greece-Recrystallization and Mobilization of Zircon During High-Pressure Metamorphism. *J. Petrol.* **2003**, *44*, 1977–2002. [CrossRef]
77. Taylor, R.J.M.; Clark, C.; Fitzsimons, I.C.W.; Santosh, M.; Hand, M.; Evans, N.; McDonald, B. Post-peak, fluid-mediated modification of granulite facies zircon and monazite in the Trivandrum Block, southern India. *Contrib. Mineral. Petrol.* **2014**, *168*, 1–17. [CrossRef]
78. Taylor, R.J.M.; Kirkland, C.L.; Clark, C. Accessories after the facts: Constraining the timing, duration and conditions of high-temperature metamorphic processes. *Lithos* **2016**, *264*, 239–257. [CrossRef]
79. Peterman, E.M.; Snoeyenbos, D.R.; Jercinovic, M.J.; Kylander-Clark, A. Dissolution-reprecipitation metasomatism and growth of zircon within phosphatic garnet in metapelites from western Massachusetts. *Am. Mineral.* **2016**, *101*, 1792–1806. [CrossRef]
80. Soman, A.; Geisler, T.; Tomaschek, F.; Grange, M.; Berndt, J. Alteration of crystalline zircon solid solutions: A case study on zircon from an alkaline pegmatite from Zomba-Malosa, Malawi. *Contrib. Mineral. Petrol.* **2010**, *160*, 909–930. [CrossRef]
81. Yardley, B.W.D.; Graham, J.T. The origins of salinity in metamorphic fluids. *Geofluids* **2002**, *2*, 249–256. [CrossRef]
82. Burger, H.; Peck, W.; Johnson, K.; Tierney, K.; Pouslen, C.; Cady, P.; Lowell, J.; MacFarlane, W.; Sincock, M.; Archuleta, L.; et al. Geology and geochemistry of the Spuhler Peak Metamorphic Suite. *Geol. Soc. Am. Spec. Pap.* **2004**, *377*, 47–70. [CrossRef]